

Numerical evolution of squeezed and non-Gaussian states in loop quantum cosmology

Peter Diener^{1,2,*}, Brajesh Gupt^{2,†}, Miguel Megevand^{2,‡} and Parampreet Singh^{2,§}

¹ *Center for Computation and Technology, Louisiana State University, Baton Rouge, LA 70803, U.S.A. and*

² *Department of Physics and Astronomy, Louisiana State University, Baton Rouge, LA 70803, U.S.A.*

In recent years, numerical simulations with Gaussian initial states have demonstrated the existence of a quantum bounce in loop quantum cosmology in various models. A key issue pertaining to the robustness of the bounce and the associated physics is to understand the quantum evolution for more general initial states which may depart significantly from Gaussianity and may have no well defined peakedness properties. The analysis of such states, including squeezed and highly non-Gaussian states, has been computationally challenging until now. In this manuscript, we overcome these challenges by using the Chimera scheme for the spatially flat, homogeneous and isotropic model sourced with a massless scalar field. We demonstrate that the quantum bounce in this model occurs even for states which are highly squeezed or are non-Gaussian with multiple peaks and with little resemblance to semi-classical states. The existence of the bounce is found to be robust, being independent of the properties of the states. The evolution of squeezed and non-Gaussian states turns out to be qualitatively similar to that of Gaussian states, and satisfies strong constraints on the growth of the relative fluctuations across the bounce. We also compare the results from the effective dynamics and find that, although it captures the qualitative aspects of the evolution for squeezed and highly non-Gaussian states, it always underestimates the bounce volume. We show that various properties of the evolution, such as the energy density at the bounce, are in excellent agreement with the predictions from an exactly solvable loop quantum cosmological model for arbitrary states.

I. INTRODUCTION

Over the past decade, loop quantum cosmology (LQC) has proved to be a promising avenue to address the problem of classical singularities, providing a consistent framework to gain insights on the physics at the Planck scale [1]. LQC is a symmetry reduced canonical quantization of homogeneous spacetimes using the techniques of loop quantum gravity (LQG) where the underlying geometry is discrete. This quantum discreteness of geometry results in an upper bound on the curvature of spacetime which leads to the absence of singularities in LQC. The main feature of the singularity resolution in LQC is the replacement of the big bang singularity by a quantum bounce. Resulting from the non-perturbative quantum gravitational effects, the quantum bounce establishes a non-singular bridge between the disjoint expanding and contracting branches of the classical theory [2–4]. The robustness of the singularity resolution has been studied in great detail for various cosmological models [3–12], including in the presence of potentials [13, 14] and anisotropies [15–19]. For all the models where numerical simulations have been performed, the evolution of semi-classical states has been shown to be free of the classical singularities, and the occurrence of a quantum bounce has been established.¹ The spatially flat homogeneous Friedmann-Robertson-Walker (FRW) model with a massless scalar field can also be solved exactly in LQC. This quantization known as solvable LQC (sLQC) [22], predicts the existence of a universal maximum for the expectation value of the energy density and a bounce for all the states in the physical Hilbert space. This model has been used to obtain powerful constraints on the growth of the relative fluctuations across the bounce [23–26], and to compute a consistent quantum probability for the occurrence of a bounce (which turns out to be unity) [27].

Due to the underlying quantum geometry, the quantum Hamiltonian constraint in isotropic models in LQC is a finite difference equation in volume. This is in contrast to the Wheeler-DeWitt quantization where the corresponding quantum Hamiltonian constraint is a differential equation. In the cases where the matter part is considered to be a massless scalar field, the latter serves as a good internal clock to measure the variation in the volume of the universe and the evolution can be studied following a rigorous quantization. In contrast to LQC where the quantum evolution is non-singular and physical states undergo a quantum bounce, the Wheeler-DeWitt quantization of this model does

* diener@cct.lsu.edu

† brajesh@phys.lsu.edu

‡ megevand@phys.lsu.edu

§ psingh@phys.lsu.edu

¹ For a review of various numerical methods in LQC, see Ref. [20, 21].

not resolve the classical singularity, and the physical states follow the classical trajectories all the way to the big bang singularity in the backward evolution, or the big crunch singularity in the forward evolution. At curvature scales much smaller than the Planck scale, the discrete quantum geometry leads to the classical geometry and the difference equation in LQC is well approximated by the Wheeler-DeWitt differential equation. Therefore, in the low curvature regime, the trajectories of LQC, Wheeler-DeWitt theory and classical general relativity are in extremely good agreement. Interestingly, there also exist effective descriptions of discrete quantum evolution in LQC, which for suitably chosen sharply peaked states can capture the underlying quantum evolution extremely well all the way to the quantum bounce [28]. Note that for the effective description, the underlying geometry is a continuum geometry but is only classical at scales much smaller than the Planck curvature. The effective dynamics for the spatially flat model results in a modified Friedmann equation where the dominant modification is encoded in the ρ^2 correction [4, 29], and has been extensively used to extract phenomenological predictions in LQC [1].

One of the main goals of earlier work in LQC was to demonstrate the existence of a quantum bounce for Gaussian states which are sharply peaked at classical trajectories in a macroscopic universe at late times. For the massless scalar field model in the spatially flat isotropic and homogeneous spacetime, this implies that the initial state is peaked at a large value of the field momentum and at a large volume. For such states, the quantum bounce was found to occur approximately at an energy density $\rho \approx \rho_{\max}$ where $\rho_{\max} \approx 0.409\rho_{\text{Pl}}$ is the universal maximum of energy density predicted in sLQC [22].² Numerical simulations of initial states which are sharply peaked also demonstrated an excellent agreement between the quantum evolution and the trajectory obtained from the effective Hamiltonian constraint. To establish the robustness of new physics at the Planck scale, it is important to understand the quantum evolution of states which are not sharply peaked and depart from Gaussianity. Such states may be widely spread, squeezed and multi-peaked with no semi-classical properties. Though such states do not lead to a classical macroscopic universe at late times, they are important for testing the genericity of predictions and also hold significance for some phenomenological reasons, such as the understanding of the role of non-Gaussianities on the cosmological perturbations in a loop quantum universe. A first step in this direction was performed recently in Ref. [30], where quantum evolution of widely spread Gaussian states in the spatially flat homogeneous and isotropic model sourced with a massless scalar field were extensively studied. These simulations were performed using the Chimera scheme [31], which has been recently proposed to overcome computational difficulties associated with the evolution of widely spread states. It was found that the qualitative features of the quantum bounce remain true for the widely spread states. However, there are quantitative differences between the LQC and the corresponding effective trajectories. A general feature of these differences, is that the effective theory always underestimates the bounce volume and overestimates the energy density at the bounce.

In this article we test the robustness of the quantum bounce by considering non-Gaussian states in the quantization of homogeneous and isotropic spatially flat spacetime with a massless scalar field as given in Ref. [4].³ Non-Gaussian states present computational challenges far more severe than the corresponding Gaussian states. To understand this, let us take an example of a squeezed state. It turns out that for the same value of field momentum and its absolute dispersion, the squeezed state is more widely spread in volume than its Gaussian counterpart. A typical simulation for a sharply peaked initial state with $p_\phi = 1000\sqrt{G}\hbar$ and relative dispersion in volume observable of 1% requires about 30,000 grid points on the spatial grid. Such a simulation takes approximately 240 sec on a 2.4 GHz Sandybridge workstation with 16 cores. On the other hand, a simulation of a squeezed state with the same values of field momentum has larger volume dispersion and requires 4×10^{11} grid points. Such a simulation, running on a computer equipped with enough memory for the entire simulation, would take approximately 7×10^{12} hrs $\approx 10^8$ years with pre-Chimera techniques. As for the widely spread states considered in Ref. [30], the Chimera scheme dramatically brings down the computational costs and makes such simulations possible. The Chimera scheme utilizes the fact that in the large volume limit, the quantum Hamiltonian constraint in LQC can be very well approximated by the Wheeler-DeWitt equation [31]. In this scheme a hybrid (spatial) grid is introduced. The hybrid grid is composed of an inner grid corresponding to the small volume regime, where we solve the LQC difference equation, and an outer grid where the evolution is governed by the Wheeler-DeWitt differential evolution equation. The inner grid, of course, has to be chosen sufficiently large to capture all the non-trivial LQC physics. This leads to a significant reduction in the computational cost of the simulation. A simulation of the squeezed state mentioned above, that would have taken 10^8 years, can now be performed in about 10 minutes.

Using the Chimera scheme we perform numerical simulations of a spatially flat isotropic and homogeneous model in LQC in the presence of a massless scalar field with three types of non-Gaussian states: (i) squeezed states (ii) a sum of Gaussians in the momentum space which lead to a multi-peaked state in volume, and (iii) a state with even more peaks. The two latter types of states will be denoted multi-peaked-1 and multi-peaked-2 in this manuscript. We

² Strictly speaking, the energy density at which the quantum bounce occurs, never saturates the upper bound ρ_{\max} in sLQC. For the sharply peaked states, the bounce density is extremely close to but less than ρ_{\max} [4, 30], and for the widely spread states the bounce density can be much smaller [26, 30].

³ For a comparison of different quantizations of this model in LQC, see Ref. [32]

find, as in the earlier studies with Gaussian states in this model [3, 4, 30], that the evolution is non-singular, and the classical singularity is replaced by a quantum bounce. This is shown to be a generic feature of all the types of states considered, irrespective of the initial parameters. The relative dispersions across the bounce, for all types of states *always* obey the triangle inequalities derived in Ref. [24]. We also find that certain types of squeezed states satisfy a stronger set of triangle inequalities as derived in Ref. [25] for sharply peaked states. If the state is highly squeezed then this particular triangle inequality is found to be violated. The latter inequality is also satisfied by multi-peaked states studied in this work, even though they are not sharply peaked. The reason for this lies in the way these states are constructed and the values of parameters considered.⁴ These results confirm the robustness of the constraints on the growth of relative fluctuations across the bounce for highly non-Gaussian states. We find that the profile of the state at early times before the bounce is not affected at late times after the bounce. In synergy with the results obtained in Ref. [30], our analysis reveals that the effective theory always underestimates the bounce volume and overestimates the energy density at the bounce. Since the effective dynamics is derived under the assumptions of sharply peaked Gaussian states, we find, as expected, significant quantitative departures between the predictions of the effective theory and the quantum evolution of states with large volume dispersion. However, the effective dynamics qualitatively captures the main features of the physics in LQC, and it still provides a very good approximation to the underlying quantum dynamics for states with small dispersion, even when they are highly non-Gaussian. We find that the energy density can be much smaller than the maximum density predicted in sLQC. In particular, for squeezed states, we find that the behavior of the energy density with increased squeezing agrees extremely well with the analytical calculations performed for sLQC in Ref. [26]. It is important to note that the quantum constraint considered in our analysis, which is the same as the one analyzed in Ref. [4], does not correspond to the one in sLQC. Despite this difference, we find sLQC to provide important insights on various findings and in agreement with several results in our analysis.

Finally, it is worth emphasizing that, although the states studied here do not necessarily correspond to a classical universe at late times, they are in the physical Hilbert space. Therefore, their study is important for testing the robustness of the Planck scale physics, in particular the resolution of the classical singularity, the existence of a quantum bounce, constraints on the growth of fluctuations and the reliability of the effective dynamics. Our results show that many features of the new physics first observed for the Gaussian states also hold true for the states which are highly non-Gaussian. Thus, our analysis provides a strong robustness test of the physics in LQC. Furthermore, these results are potentially important in computing corrections to the observational signatures of LQC arising from the state fluctuations.

This manuscript is organized as follows. We give a brief overview of the loop quantization, relative fluctuations and the effective dynamics of a flat FRW model with a massless scalar field in Sec. II. In Sec. III A, we describe the construction of the three different types of non-Gaussian initial states. For completeness we briefly discuss the main features of the Chimera scheme in Sec. III B. In Sec. IV we discuss the results of the numerical simulations for the three kinds of states and also compare their LQC evolution with the corresponding effective trajectories. We also study the variation of the energy density at the bounce and the validity of the triangle equalities for the relative fluctuations of various non-Gaussian states. In Sec. V we present a summary and discussion of the main results.

II. LOOP QUANTUM COSMOLOGY OF THE SPATIALLY FLAT MODEL: QUANTUM CONSTRAINT, FLUCTUATIONS AND EFFECTIVE DYNAMICS

In this section we briefly describe the loop quantization of a flat FRW spacetime with a massless scalar field as the matter source. We start with a summary of the key ideas behind the quantum Hamiltonian constraint in LQC and the way the difference equation arises. After discussing the relation of the LQC quantum constraint with the Wheeler-DeWitt equation at small spacetime curvatures, we summarize the main results on the bounds of relative fluctuations of the Dirac observables across the bounce. We conclude this section with a discussion of the effective dynamics derived from the effective Hamiltonian for sharply peaked Gaussian states [28]. For details, we refer the reader to the original works where this quantization was first performed [3, 4] (see also Ref. [22]) and Ref. [1] for a review.

⁴ All the states considered in this manuscript are constructed using “method-3” of Refs. [4, 30]. In this method, the initial state uses Wheeler-DeWitt eigenfunctions but with an additional phase factor, carefully chosen to mimic the behavior of eigenfunctions of LQC at large volumes. Depending on the parameters of the state, in this construction, the relative fluctuations of volume at times much earlier and much later after the bounce can be very similar. If a multi-peaked state has this behavior, the stronger form of triangle inequality (2.20) can be satisfied.

A. Quantum Hamiltonian Constraint

Loop quantization of the cosmological spacetimes is based on the techniques of LQG, where the primary variables for the quantization of the gravitational sector are the holonomies of the Ashtekar-Barbero connection A_a^i and the fluxes of the triads E_i^a . In this canonical quantization, due to the homogeneity of the cosmological spacetimes, the only non-trivial constraint is the Hamiltonian constraint which is expressed in terms of the symmetry reduced version of the canonically conjugate connection-triad pair (c, p)

$$A_a^i = c V_o^{1/3} \hat{\omega}_a^i, \quad \text{and} \quad E_i^a = p V_o^{-2/3} \sqrt{q} \hat{e}_i^a, \quad (2.1)$$

where \hat{e}_i^a are the densitized triads and $\hat{\omega}_a^i$ are the fiducial co-triads compatible with the fiducial metric \hat{q}_{ab} , and V_o denotes the volume of the fiducial cell introduced to define the symplectic structure in the canonical quantization. At the kinematical level, the triad is related to the scale factor in the physical metric as $|p| = V_o^{1/3} a^2 = V^{2/3}$, where the modulus sign arises due to the two possible orientations of the triads.⁵ For the classical solutions, the connection is proportional to the time derivative of the scale factor $c = \gamma V_o^{1/3} \dot{a}$, where $\gamma \approx 0.2375$ is the Barbero-Immirzi parameter and the derivative is taken with respect to proper time.

The gravitational part of the Hamiltonian constraint expressed in terms of the triads and the field strength F_{ab}^i of the connection is

$$C_{\text{grav}} = -\frac{1}{\gamma^2} \int d^3x \varepsilon_{ijk} \frac{E^{ai} E^{bj} F_{ab}^k}{\sqrt{|\det(\mathbf{E})|}}, \quad (2.2)$$

where we have chosen the lapse to be unity. For the massless scalar field model under consideration, the matter part of the Hamiltonian constraint is

$$C_{\text{matt}} = \frac{p_\phi^2}{2|p|^3}, \quad (2.3)$$

where p_ϕ is the momentum of the scalar field, which is a constant of motion in this case.

To quantize the Hamiltonian constraint, the field strength is expressed in terms of the holonomies $h_i^{(\lambda)}$ of the symmetry reduced connection c on a square loop \square_{ij}

$$F_{ab}^i = -2 \lim_{Ar_\square \rightarrow 0} \text{Tr} \left(\frac{h_{\square_{jk}}^{(\lambda)} - 1}{Ar_\square_{ij}} \right) \tau^k \hat{\omega}_a^j \hat{\omega}_b^k, \quad (2.4)$$

where $h_{\square_{ij}}^{(\lambda)} = h_i^{(\lambda)} h_j^{(\lambda)} (h_i^{(\lambda)})^{-1} (h_j^{(\lambda)})^{-1}$, and Ar_\square denotes the physical area of the loop whose sides are parameterized by λ . In LQC, this area has a minimum value determined by the underlying quantum geometry which fixes λ as $\lambda = 2\sqrt{(\sqrt{3}\pi\gamma)} l_{\text{Pl}}$. The non-local nature of the field strength which encodes the quantum geometry plays an important role in the new physics near the Planck scale in LQC. The elements of the holonomy algebra are almost periodic functions of the connection, and the corresponding operators act as a translation

$$\exp(\widehat{i\lambda b/2}) |v\rangle = |v-1\rangle, \quad (2.5)$$

where $b = c/|p|^{1/2}$ and $|v\rangle$ is the eigenstate of the volume operator

$$\hat{V}|v\rangle = \left(\frac{8\pi\gamma}{6} \right)^{3/2} \frac{|v|}{K} l_{\text{Pl}}^3 |v\rangle, \quad K = \frac{2}{3\sqrt{3}\sqrt{3}}. \quad (2.6)$$

The resulting action of the Hamiltonian constraint on states $\Psi(v, \phi)$ is

$$\widehat{C}_{\text{grav}} \Psi(v, \phi) = C^+(v) \Psi(v+4, \phi) + C^o(v) \Psi(v, \phi) + C^-(v) \Psi(v-4, \phi), \quad (2.7)$$

⁵ Since the matter sector of the Hamiltonian constraint in this model has no fermions, the resulting physics is insensitive to the orientation of the triad.

where the coefficients C^\pm and C^o are given by

$$\begin{aligned} C^-(v) &= C^+(v-4) = \frac{3\pi KG}{8} |v-2| \left| |v-3| - |v-1| \right|, \\ C^+(v) &= \frac{3\pi KG}{8} |v+2| \left| |v+1| - |v+3| \right|, \\ C^o(v) &= -C^+(v) - C^-(v). \end{aligned} \quad (2.8)$$

The total Hamiltonian constraint can thus be expressed as a Klein-Gordon type equation with ϕ as the internal time:

$$\frac{\partial^2}{\partial \phi^2} \Psi(v, \phi) = -\hat{\Theta} \Psi(v, \phi). \quad (2.9)$$

The operator $\hat{\Theta}$ is the LQC difference operator, which is positive definite and self-adjoint, and is defined as follows:

$$\hat{\Theta} = -\frac{1}{B(v)} \left[C^+(v) \Psi(v+4, \phi) + C^o(v) \Psi(v, \phi) + C^-(v) \Psi(v-4, \phi) \right], \quad (2.10)$$

where

$$B(v) = \frac{27}{8} K |v| \left| |v+1|^{1/3} - |v-1|^{1/3} \right|^3 \quad (2.11)$$

denotes the eigenvalues of the inverse volume operator in LQC. If we label the eigenvalues of $\hat{\Theta}$ with ω^2 , then the physical states can be either chosen as the positive frequency ($\omega > 0$) or the negative frequency ($\omega < 0$) solutions. During the evolution there is no mixing between positive and negative frequencies, and it suffices to consider only positive frequency states. These states are normalized using the following inner product obtained by using group averaging procedure [33, 34]

$$\langle \Psi_1 | \Psi_2 \rangle = \sum_v \overline{\Psi_1}(v, \phi_o) B(v) \Psi_2(v, \phi_o). \quad (2.12)$$

This inner product can also be obtained by requiring that the action of Dirac observables in this model are self adjoint. Two Dirac observables we will be interested in particularly are the volume at a given slice of time ϕ , and the field momentum, which is a constant of motion

$$\hat{V}|_{\phi_o} \Psi(v, \phi) = \left(\frac{8\pi\gamma}{6} \right)^{3/2} \frac{l_{\text{Pl}}^3}{K} |v| e^{i\sqrt{\Theta}(\phi-\phi_o)} \Psi(v, \phi_o), \quad \text{and} \quad \hat{p}_\phi \Psi(v, \phi) = -i\hbar \partial_\phi \Psi(v, \phi) = \sqrt{\Theta} \Psi(v, \phi). \quad (2.13)$$

We can evaluate the expectation values of the Dirac observables as follows

$$\langle \hat{\mathcal{O}} \rangle = \langle \Psi | \hat{\mathcal{O}} | \Psi \rangle = \|\Psi\|^{-1} \sum_v B(v) \overline{\Psi}(v, \phi) \hat{\mathcal{O}} \Psi(v, \phi) \quad (2.14)$$

where $\|\Psi\|$ is the norm of the wavefunction and $\hat{\mathcal{O}}$ refers to the quantum operator of interest. The quantum evolution and the action of the Dirac observables preserves the lattice in volume labeled by ϵ : $v = \pm\epsilon + 4n$, where $\epsilon \in [0, 4)$ and $n \in \mathbb{Z}$. Due to this reason, there is a superselection and the physical Hilbert space can be decomposed into separable Hilbert spaces labeled by ϵ , \mathcal{H}_ϵ . In our analysis, we will consider the choice $\epsilon = 0$, since it allows the zero volume. Finally, since there are no fermions in our model, the physical states will be considered to be symmetric under the change of sign of the physical triads: $\Psi(v, \phi) = \Psi(-v, \phi)$.

The evolution operator in LQC (eq. (2.10)) is a non-singular difference operator with a uniform discretization in v which results in a quantum bounce of the physical states in the Planck regime [3, 4]. The existence of a bounce is tied to the underlying quantum geometry which is captured by the non-local nature of the field strength in the quantum Hamiltonian constraint. In contrast, in the Wheeler-DeWitt theory, the quantization of this model yields the following evolution equation:

$$\frac{\partial^2}{\partial \phi^2} \underline{\Psi}(v, \phi) = -\hat{\underline{\Theta}} \underline{\Psi}(v, \phi) = 12\pi G v \frac{\partial}{\partial v} \left(v \frac{\partial}{\partial v} \right) \underline{\Psi}(v, \phi), \quad (2.15)$$

where the operator $\hat{\underline{\Theta}}$ is the Wheeler-DeWitt evolution operator with eigenvalues ω^2 . The evolution of the physical states in the Wheeler-DeWitt theory does not lead to a singularity resolution. Rather, the states follow the classical trajectory throughout the evolution. In the large volume approximation, it is straightforward to show that $\hat{\underline{\Theta}}$ can be approximated by $\hat{\underline{\Theta}}$. Thus, the continuum classical geometry is recovered from LQC at small spacetime curvature. This property turns out to be extremely useful in our numerical simulations.

B. Properties of the dispersion in p_ϕ and V .

An important property of the loop quantum evolution is that the relative fluctuations of volume observables are very tightly constrained across the bounce by the dispersion in the momentum observable [23–26]. This implies that semi-classicality of the initial state is preserved through the evolution. This property is most evident in terms of the triangle inequalities, which constrain the change in the relative fluctuations in volume in the expanding and contracting phases of LQC with the relative fluctuation in the momentum p_ϕ . Note that the latter and its fluctuation remains constant throughout the evolution. The triangle inequalities are derived using sLQC [22], which is an exactly solvable loop quantization of the massless scalar model in the spatially flat homogeneous spacetime with the lapse $N = a^3$. The most general treatment valid for all the physical states in sLQC is performed in Ref. [24], which reaches the conclusion that although the volume dispersions $\Delta \ln(\hat{v}|_\phi)$ could be different across the bounce, the difference between their asymptotic values (σ_\pm) is bounded by the dispersion in the field momentum $\Delta \ln(\hat{p}_\phi)$ as follows⁶

$$|\sigma_+ - \sigma_-| \leq 2\sigma. \quad (2.16)$$

In the numerical simulations,

$$\sigma_\pm = \Delta \ln(\hat{v}|_\phi)_\pm, \quad \text{and} \quad \sigma = \Delta \ln(\hat{p}_\phi/\sqrt{G\hbar}) \quad (2.17)$$

are measured at very large values of $|\phi|$ before and after the bounce. Since the derivation of (2.16) assumes no particular state, it is valid for all the choices of initial states in the physical Hilbert space, irrespective of whether the state is sharply peaked or not. A stronger bound on the fluctuations can be obtained by noting that if a state is sharply peaked, then the dispersion in the logarithm of a physical observable \mathcal{O} can be approximated as $\langle \Delta \ln \hat{\mathcal{O}} \rangle \approx \langle \Delta \hat{\mathcal{O}} \rangle / \langle \hat{\mathcal{O}} \rangle$. Under this approximation we can write

$$\Delta(\ln(\hat{v}|_\phi)_\pm) \approx \Sigma_\pm := \left(\frac{\langle \Delta \hat{v}|_\phi \rangle}{\langle \hat{v}|_\phi \rangle} \right)_\pm \quad \text{and} \quad \Delta \ln(\hat{p}_\phi/\sqrt{G\hbar}) \approx \Sigma := \frac{\langle \Delta \hat{p}_\phi \rangle}{\langle \hat{p}_\phi \rangle}. \quad (2.18)$$

The inequality in eq. (2.16) then takes the following form

$$|\Sigma_+ - \Sigma_-| \leq 2\Sigma, \quad (2.19)$$

which can also be written as

$$\mathcal{E} := \frac{|\Sigma_+ - \Sigma_-|}{2\Sigma} \leq 1. \quad (2.20)$$

Unlike (2.16), the inequality (2.20) is valid when a state satisfies (2.18). When the latter approximation is not satisfied, the inequality (2.20) can be violated, as we show in our analysis for highly squeezed states which have large relative fluctuation in volume. However, depending on the construction of states and the values of parameters, it is possible that \mathcal{E} turns out to be smaller than unity even if the state may not be sharply peaked. Examples of such states are studied in Sec. IVB and Sec. IVC, where due to a peculiar behavior of Σ_\pm tied to the way states are constructed, the above inequality is satisfied for certain parameters for multip peaked states. It is important to note that in contrast to (2.20), the triangle inequality (2.16) is satisfied for all the physical states independent of the choice of parameters and the way they are constructed.

These triangle inequalities imply that the difference between the relative dispersions across the bounce for a semi-classical state is tightly constrained, and the semi-classicality of a state across the bounce is preserved. That is, if the wavefunction of the universe on one side of the bounce is semi-classical then it will remain semi-classical throughout the evolution. This is an important argument in support of cosmic recall [23]. Since the triangle inequalities (2.16) are derived in sLQC, at first it may seem surprising that they are found to be satisfied for all the states in the present analysis, where the quantum constraint is different from the exactly solvable model in sLQC. The reason for this agreement lies in the fact that the physical differences between sLQC and the presented quantization can only become important when the bounce volume is close to the Planck volume, which never occurs for any state considered in our analysis.

⁶ The expectation value of the logarithm of field momentum can be computed analytically in this model using $\langle \ln(\hat{p}_\phi/\sqrt{G\hbar}) \rangle = \|\Psi(\omega)\|^{-1} \int \bar{\Psi}(\omega) \ln(\omega/\sqrt{G}) \Psi(\omega) d\omega$.

C. Effective dynamics

For suitably chosen physical states, it is possible to derive a continuum effective spacetime description of LQC via the geometric formulation of quantum mechanics, where the Hilbert space is treated as a quantum phase space. In this manuscript, we will analyze effective dynamics as obtained in the embedding approach, where one finds a faithful embedding of the quantum phase space into the classical phase space [28, 35].⁷ The effective Hamiltonian constraint can then be derived through an appropriate choice of a semi-classical state, such as a sharply peaked Gaussian state. Using Hamilton's equations, modified Friedmann and Raychaudhuri equations with quantum geometric corrections can then be obtained in a straightforward way. The effective Hamiltonian constraint for the spatially flat, homogeneous and isotropic FRW spacetime sourced with a massless scalar field is given as [28]⁸

$$C_{\text{eff}} = -\frac{3V}{8\pi G\gamma^2} \frac{\sin^2(\lambda b)}{\lambda^2} + \frac{p_\phi^2}{2V} \approx 0. \quad (2.21)$$

The variable $b = c/|p|^{1/2}$ is the conjugate variable to V and satisfies the Poisson bracket relation: $\{b, V\} = 4\pi G\gamma$, where $\lambda^2 = 4\sqrt{3}\pi\gamma l_{\text{Pl}}^2$ is the minimum eigenvalue of the area operator in loop quantum cosmology. This effective Hamiltonian constraint neglects any state dependent fluctuation terms, which are small for sharply peaked states with small relative fluctuations. For a more accurate analysis, these terms should be included for a given choice of semi-classical states. For states which are not semi-classical or have large relative fluctuations, the underlying assumptions in the derivation of the effective Hamiltonian are violated and the effective dynamics can not be trusted. In this manuscript, we will restrict our analysis to the study of the effective dynamics resulting from eq.(2.21).

Using Hamilton's equation of motion for the volume variable V , one can obtain the time derivative of V as follows

$$\dot{V} = \frac{3}{2\gamma\lambda} \sin(2\lambda b) V. \quad (2.22)$$

This equation, along with the vanishing of the Hamiltonian constraint, yields the modified Friedmann equation

$$H^2 = \left(\frac{\dot{V}}{3V}\right)^2 = \frac{8\pi G}{3} \rho \left(1 - \frac{\rho}{\rho_b^{\text{eff}}}\right), \quad \text{where} \quad \rho_b^{\text{eff}} = \frac{3}{8\pi G\gamma^2\lambda^2} \approx 0.409 \rho_{\text{Pl}}. \quad (2.23)$$

Here $H = \dot{V}/3V = \dot{a}/a$ is the Hubble rate and $\rho = p_\phi^2/(2V^2)$ is the energy density of the scalar field. The modified Friedmann equation predicts a maximum bound for energy density ρ_b^{eff} where the Hubble rate vanishes and a quantum bounce occurs. It is interesting to note that this bound is the same as the maximum bound ρ_{max} for the expectation values of the energy density observable in sLQC. However, unlike in sLQC, where the bound is valid for all the states in the physical Hilbert space, the bound in energy density in the effective dynamics is derived for sharply peaked Gaussian states.

The modified Raychaudhuri equation can in a similar way be derived from the time derivative of b , giving

$$\frac{\ddot{a}}{a} = \frac{-4\pi G}{3} \rho \left(1 - 4\frac{\rho}{\rho_b^{\text{eff}}}\right) - 4\pi G P \left(1 - 2\frac{\rho}{\rho_b^{\text{eff}}}\right). \quad (2.24)$$

The modified Friedmann and Raychaudhuri equations given in equations (2.23) and (2.24) respectively lead to the classical Friedmann and Raychaudhuri equation when $\rho \ll \rho_b^{\text{eff}}$. These equations can be used to obtain the effective dynamical trajectory of a cosmological model by providing initial conditions at some $t = t_0$. In this paper we compute the effective dynamical trajectories corresponding to an LQC evolution by giving the initial conditions far from the bounce in the low curvature regime in the expanding branch.

For sharply peaked initial states, extensive numerical simulations for different matter models show that the effective dynamics provides an excellent description of the underlying quantum dynamics (see Ref. [1, 21] for a review of these results). For states which are not sharply peaked, there are additional corrections to the effective Hamiltonian constraint which affect the energy density in the effective theory at the bounce. A detailed numerical analysis of widely spread Gaussian states has been recently performed in Ref. [30]. It was concluded that, for states with significant relative fluctuations, even though the effective dynamical trajectory obtained from the above constraint

⁷ For a discussion of different approaches to obtain effective dynamics in LQC, see [1].

⁸ In the effective Hamiltonian, we ignore the contributions from the inverse volume effects (encoded in $B(v)$ (eq.2.11)). These corrections play little role on the physical implications in LQC unless the bounce occurs close to the Planck volume.

captures the qualitative features of the underlying quantum dynamics, it always overestimates the spacetime curvature at the bounce. In our analysis, we will test the validity of the effective Hamiltonian constraint for states which are non-Gaussian. We will show that for states which are highly non-Gaussian, there are large departures between the quantum evolution and the above effective dynamics. It is important to note that, though the evolution of such highly non-Gaussian states can not be reliably captured by the effective dynamics, it turns out to be in excellent agreement with predictions from sLQC. This is not surprising because the predictions extracted from sLQC are valid for arbitrary states in the physical Hilbert space, whereas the effective description assumes that the states have some peakedness properties.

III. INITIAL DATA AND NUMERICAL SCHEME

In the previous section we discussed an important relation between the quantum difference equation in LQC and the differential WDW equation in the regime of small spacetime curvature. In the spatially flat model under consideration, for a given value of the field momentum p_ϕ , the spacetime curvature becomes smaller as the volume increases. Therefore, at large volume, the eigenfunctions of LQC can be approximated by a linear superposition of the eigenfunctions of $\hat{\Theta}$ (eq.(2.15)) in the Wheeler-DeWitt theory, which are given by

$$\underline{e}_k(v) = \frac{1}{2\pi} e^{ik \ln |v|}, \quad (3.1)$$

with $\omega = \sqrt{12\pi G}|k|$. A general solution of the Wheeler-DeWitt equation can be written as a superposition of the outgoing ($k < 0$) and the incoming ($k > 0$) solutions. The outgoing part corresponds to the expanding branch, and the ingoing part corresponds to the contracting branch in the FRW spacetime. In the Wheeler-DeWitt theory, the contracting and expanding trajectories are disjoint, and the initial data can be chosen on any of the trajectories. If an initial state is chosen peaked on an expanding branch, i.e. a wavefunction with no support on the positive axis of k , its evolution in the Wheeler-DeWitt theory yields a trajectory which agrees with the classical GR trajectory all the way to the big bang singularity at $v = 0$ in its past evolution. Similarly, if the initial state is chosen on a contracting branch, it encounters a big crunch singularity in its future evolution.⁹

In our numerical simulations we will consider initial states which are peaked on the expanding trajectory at late times (i.e. large ϕ) and have $\omega > 0$. A general positive frequency Wheeler-DeWitt initial state at time $\phi = \phi_o$ is of the form

$$\underline{\Psi}(v, \phi) = \int \Psi(k) \underline{e}_k(v) e^{i\omega(\phi - \phi_o)} e^{-i\alpha} dk, \quad (3.2)$$

where $k = -p_\phi / \sqrt{12\pi G \hbar^2}$. The time derivative of $\underline{\Psi}(v, \phi)$ can be computed by evaluating the following integral

$$\frac{\partial}{\partial \phi} \underline{\Psi}(v, \phi) = \int i\omega \Psi(k) \underline{e}_k(v) e^{i\omega(\phi - \phi_o)} e^{-i\alpha} dk. \quad (3.3)$$

Given the form of a wavepacket $\Psi(k)$ (or equivalently $\Psi(\omega)$), the initial state and its derivative can be computed by numerically evaluating the integrals in eq. (3.2) and (3.3). Since the physical states are required to be symmetric under the change in the orientation of the triads, i.e. $\Psi(v, \phi) = \Psi(-v, \phi)$, we construct the initial states using the Wheeler-DeWitt eigenfunctions that approximate the symmetric eigenfunctions of the LQC operator at large volumes. This is achieved by multiplying the integrand in eq.(3.2) by a phase factor $e^{-i\alpha}$ where $\alpha = k(\ln |k| - 1)$ [4, 30].¹⁰

Before going into more details about our prescription for the initial data, it is useful to point out an important property of the eigenfunctions of the $\hat{\Theta}$ operator in the small volume regime. Earlier studies show that the eigenfunctions of $\hat{\Theta}$, unlike those of $\hat{\Theta}$, decay almost exponentially near zero volume [3, 4, 38]. The decay starts near a cutoff volume V_c , which can be computed from the analytical results in Ref. [38] as¹¹

$$V_c = \sqrt{\frac{4\pi G}{3}} \gamma \lambda \omega \hbar. \quad (3.4)$$

⁹ It may seem that a general superposition of incoming and outgoing solutions can potentially resolve the big bang singularity in the Wheeler-DeWitt theory. This expectation turns out to be wrong. It can be analytically shown that for this matter model, even with the states constructed from a superposition of expanding and contracting solutions, the probability for a singularity to occur is unity in the Wheeler-DeWitt quantization [36, 37].

¹⁰ The initial states used for the simulations in this manuscript are based on “method-3” in the convention used in earlier works [3, 30].

¹¹ In Ref. [38], the cutoff was obtained on k (see eq.(3.36a) of Ref. [38]). Since our goal will be to understand this cutoff in volume and compare it to the bounce volume, we have written the same equation in a different form.

Although V_c is computed for eigenfunctions in sLQC, one may expect that, for states with a well defined peak, a good estimation of the volume at which the wavefunction amplitude decays almost exponentially will be given by replacing ω with the eigenvalue at which the state is peaked. The reason for this is that the main contribution to the wavefunction comes from eigenstates with eigenvalues around this value. In fact, we find that for states with a well defined peak and $\langle \hat{p}_\phi \rangle = \omega^* \hbar$ (with $\omega^* = -\sqrt{12\pi G} k^*$, see eq. (3.5)), the bounce volume is very close to the cutoff volume. For states with a well defined peak for which the expectation value of the field momentum is different from ω^* , the cutoff volume for the amplitude of the wavefunction can be estimated by using $\langle \hat{p}_\phi \rangle$ in eq.(3.4). We will see in Sec.IV that the squeezed states do show a decay of the amplitude at the bounce, starting at the value of V_c estimated in this way.

An initial state $\Psi(v, \phi)|_{\phi=\phi_o}$ and its time derivative $\partial_\phi \Psi(v, \phi)|_{\phi=\phi_o}$ provide the initial data for evolution using the Chimera method, which uses the Wheeler-DeWitt theory for evolution in an outer grid corresponding to very large volumes, and the LQC quantum difference equation in an inner grid (discussed in Sec.III B). The wave profile $\Psi(k)$ corresponds to a choice of $p_\phi = p_\phi^*$, and the initial state is constructed at $v|_{\phi_o} = v^*$ with $v^* \gg 1$. In our simulations we consider three types of initial states: squeezed states, double peaked states in the k space (which in general have more than two peaks in the v space), and multipeaked states with several peaks. We will refer to the latter two types as multipeaked-1 and multipeaked-2 in the following. Note that all of these states are far more general than the Gaussian states considered in the previous numerical simulations in LQC. In the following we first discuss the construction of the initial states and then briefly summarize the numerical algorithm used in the simulations.

A. Types of initial states

(i) *Squeezed states:* These states can be written as a generalization of the Gaussian states considered in previous numerical works [3, 4, 30]. A Gaussian state is characterized by two parameters: the field momentum where the state is peaked (p_ϕ^*) for which $k^* = -p_\phi^*/\sqrt{12\pi G\hbar}$ and the spread of the Gaussian quantified by a real quantity η . Here we generalize the Gaussian to a squeezed Gaussian state by allowing η to be a complex quantity. As yet another variation we include a factor $|k|^n$, which leads to the following expression for the wavepacket in k space

$$\Psi(k) = |k|^n e^{-\eta(k-k^*)^2}, \quad (3.5)$$

where $n \in \mathbb{R}$ and $\eta \in \mathbb{C}$.

(ii) *Multipeaked-1 states:* For this type of initial data we use the sum of two separated Gaussian waveforms in k space as

$$\Psi(k) = \frac{1}{2} \left(e^{-\eta \left(k - \left(k^* + \frac{\delta k}{\sqrt{24\pi|\eta|}} \right) \right)^2} + e^{-\eta \left(k - \left(k^* - \frac{\delta k}{\sqrt{24\pi|\eta|}} \right) \right)^2} \right), \quad (3.6)$$

where $k^* = -p_\phi^*/\sqrt{12\pi G\hbar}$ and δk is a free parameter which parameterizes the separation between the two Gaussian components in k space. We will later see that the above sum of two Gaussians, when expressed as a function of v can have multiple peaks. Note that unlike the case of squeezed states, η is assumed to be real for multipeaked-1 states.

(iii) *Multipeaked-2 states:* For our second multipeaked state we choose the following waveform in the k space

$$\Psi(k) = e^{-\eta^2 \left(k - \left(k^* + \frac{\delta k}{\sqrt{24\pi|\eta|}} \right) \right)^2} \left(k - \left(k^* - \frac{\delta k}{\sqrt{24\pi|\eta|}} \right) \right)^2, \quad (3.7)$$

where $k^* = -p_\phi^*/\sqrt{12\pi G\hbar}$, δk is a free parameter and η is a real parameter. We will see later that the above state, when expressed in v space, has several local maxima. Thus, these states have no well defined peakedness property.

B. Numerical scheme

Using the numerical techniques of Ref. [3, 4] for the quantum Hamiltonian constraint eq.(2.9) it would be computationally very expensive to evolve widely spread non-Gaussian states. On one hand, for states which are not sharply peaked, large computational domains are needed. And, since the quantum difference equation in LQC has a fixed discretization, a large domain translates into a large number of grid points. On the other hand, since the characteristic mode speeds increases linearly with volume, the use of a large domain also demands a shorter time step

in order to ensure a stable evolution [31]. These two factors combine to require unfeasibly long numerical simulations for the states with large spread in volume. Fortunately, this issue can be resolved by implementing a hybrid spatial grid. This is the Chimera scheme that was presented in [31]. As shown in that work, the computation time can be reduced significantly. As an example, simulations which would take billions of years using pre-Chimera techniques can be completed in a couple of hours. Here we present a brief summary of the method, and for more details refer the reader to Ref. [31].

The main idea of the Chimera scheme is to first identify the volume at which the Wheeler-DeWitt equation is a good approximation to the LQC difference equation and then divide the entire domain into two parts: an inner grid where the LQC difference equation is solved and an outer grid where the Wheeler-DeWitt equation is solved. On the outer grid we are not restricted by the limitations imposed by LQC on the discretization as the Wheeler-DeWitt equation has a continuum limit. Therefore we can choose any suitable discretization. In particular, it is convenient to perform a change of variables $x = \ln(v)$ and discretize in x instead of v . A uniform discretization in x then translates into larger intervals Δv for larger v , reducing the number of grid points needed for large domains. Furthermore, since the characteristic speed is constant in the new coordinates, larger spatial domains no longer demand shorter time steps. Finally, we need to choose an adequate numerical scheme for the solution of the partial differential equations. Of the two implementations presented in [31], we chose, based on efficiency considerations, the Discontinuous Galerkin (DG) method with uniformly sized discrete elements in x .

After setting up the initial state peaked on an expanding classical trajectory, as explained in Sec. III A, we evolve the state backward in time (ϕ). All the simulations show the existence of a quantum bounce, and the states are evolved through the bounce until the evolution trajectory meets a contracting classical solution corresponding to a mean volume similar to that of the initial state. We compute the expectation values of various observables using eq. (2.14), with the summation in v converted to an integral on the outer grid and the upper limit of the integral set to a finite value v_{int} . The eigenfunctions of the quantum constraint in LQC are superpositions of incoming and outgoing eigenfunctions of the Wheeler-DeWitt quantum constraint. Thus, though the initial state is constructed as a purely expanding solution of the Wheeler-DeWitt equation, it is not a purely expanding solution on the LQC grid. Thus, a small part of the state will separate and evolve as a contracting mode, that is, an outgoing mode in the backward evolution. The amplitude of this mode decreases as we move the interface between the inner and outer grid to larger values of v . In our simulations we choose v_{int} small enough so that this mode is not included in the calculation of expectation values, but large enough to accurately obtain expectation values for the ingoing mode. This is achieved by performing careful convergence studies where both v_{int} and the location of the interface between the inner and outer grid are varied and convergence of the expectation values are established.

The resources used for the simulations performed in this work varied greatly from case to case due to the variety of states studied, some with much larger spread than others. Furthermore, each simulation was repeated using different resolutions in order to check convergence of the solutions. The number of grid points used in the LQC grid varied from 7500 to 60000, whereas the number of DG elements in the Wheeler-DeWitt grid varied from 40 to 653, resulting in a total domain in v that varied from 10^9 to 10^{15} . The computation time in this case ranged from a few minutes to at most two hours when running on a 2.4 GHz Sandybridge workstation with 16 processors.

IV. RESULTS

Numerical simulations of all the non-Gaussian states considered in our analysis demonstrate the existence of a quantum bounce. When the spacetime curvature is very small, the quantum trajectory (defined by the expectation value of the volume and the internal time) agrees quite well with a classical trajectory. This agreement persists as long as the energy density ρ is very small compared to the density at the bounce ρ_b . The departures between the LQC and the classical trajectory (or the Wheeler-DeWitt trajectory) becomes significant once the energy density becomes greater than about one percent of the bounce density. As the backward evolution is continued, due to the quantum geometric effects, the evolution in LQC is non-singular, whereas the classical trajectory encounters a big bang singularity. The occurrence of a quantum bounce for all the states considered in this paper provides a strong numerical evidence in favor of the generic occurrence of the quantum bounce and is in agreement with the predictions of the exactly solvable model [22],

We present the representative results of over 100 simulations performed by studying the numerical evolution of the three different classes of non-Gaussian states described in Sec. III A. We have considered a wide variety of initial parameters for squeezed states with various values of n (where n is the exponent of the wavenumber k in eq. (3.5)) and other non-Gaussian states with various $\omega^* = -\sqrt{12\pi G} k^* = p_\phi^*/\hbar$. A summary of some of the representative simulations performed for each class of initial states is presented in Table I. In this table, we show the expectation value of the field momentum ($\langle \hat{p}_\phi \rangle$), the time of bounce (ϕ_b), the bounce volume in LQC (V_b) and the bounce volume in the effective theory ($V_b^{(\text{eff})}$) for several values of ω and the complex valued η (with the real part denoted as η_r and

TABLE I. Summary of the representative simulations shown in various figures in this paper. All the values are in Planck units.

ω^*	η_r	η_i	$\langle \hat{p}_\phi \rangle$	ϕ_b	V_b	$V_b^{(\text{eff})}$	Fig.
Squeezed, $n = 0$							
1000	0.0001	0.0001	1000	-0.7830	1109.3	1105.2	7(a)
1000	0.0001	0.001	1000	-0.7785	1336.3	1105.2	7(b)
500	0.0001	0.001	500	-0.8865	667.22	552.58	–
1000	0.01	0.01	1000	-0.7831	1611.2	1105.2	7(c)
60	0.01	0.01	60	-1.233	96.729	66.310	7(d)
Squeezed, $n = 50$							
1000	0.0003	0.0003	1077.4	-0.7366	1204.3	1190.7	8(a)
500	0.0003	0.0003	632.07	-0.8164	706.63	698.54	–
50	0.03	0.03	63.219	-2.611	221.22	69.867	8(b)
Multipeaked-1							
1000	0.0002	0	1000	-0.7835	1108.7	1105.2	11(a)
50	0.02	0	50	-1.271	78.231	55.258	11(b)
Multipeaked-2							
1000	0.0001	0	1000	-0.7835	1121.1	1105.2	15(a)
200	0.0025	0	200	-1.796	318.85	221.03	15(b)

the imaginary part denoted as η_i) for the three types of non-Gaussian states discussed in the previous section.¹² It should be noted that the values of ω^* and $\langle \hat{p}_\phi \rangle$ are the same for the squeezed states with $n = 0$, multipeaked-1 and multipeaked-2 states, while the value of $\langle \hat{p}_\phi \rangle$ is greater than that of ω^* for $n = 50$. This can be easily understood by noting that it is only the latter kind of states which are asymmetric around k^* in k space. Numerical simulations show that $\langle \hat{p}_\phi \rangle$ is a constant of motion in all cases. An important feature of all the simulations is that the bounce volume in the effective theory is smaller than in the LQC evolution. A similar feature was also observed in the recent numerical study in Ref. [30] of Gaussian states.

In the following, we will study the way the profile of a given initial wavefunction evolves across the quantum bounce, compare the trajectory given by the expectation value of the volume observable in LQC with the corresponding effective trajectory obtained from the effective Hamiltonian and investigate the properties of the dispersion in the matter and volume observables for various choices of parameters and types of initial state. The properties of the dispersion are directly related to the validity of the triangle inequalities which strongly constrain the growth of the relative fluctuations of volume and momentum observables across the bounce. We analyze our numerical results in the light of two different formulations of the triangle inequalities, as described in Sec. II B. We also study the way the energy density behaves during the evolution and compare our numerical results with the analytical results obtained in the Refs. [25, 26] for the squeezed states. Note that in the discussion of results from our analysis, data points in all the figures are plotted in Planck units and we have chosen the notation $V = \langle \hat{V} | \phi \rangle$ and $\Delta V = \langle \Delta \hat{V} | \phi \rangle$, and will continue to do so in the rest of the paper when discussing the evolution trajectories of the expectation value of the volume observable.

A. Squeezed States

The squeezed states considered in this paper are obtained by evaluating the integral in eq.(3.2) with $\Psi(k)$ given by eq.(3.5). The squeezedness of the wavefunction is controlled by the real and the imaginary parts of the complex parameter η : η_r and η_i . In the case of Gaussian states, the parameter η is real, hence the dispersion of the state can be varied relative to that of a Gaussian state for the same η_r by varying η_i . For example, for a given value of η_r for which the corresponding Gaussian state is sharply peaked, the squeezed state can be made widely spread by varying η_i . In the following we present a detailed study of the numerical evolution of squeezed states for various initial parameters ω^* and η . In our numerical analysis, several values of n were chosen and the results are qualitatively similar. Here

¹² In this section, results are discussed in terms of the physical volume of the fiducial cell which is related to v in the quantum difference equation via eq.(2.6)).

we discuss only two representative cases: $n = 0$ and $n = 50$. In the following subsections, we first highlight the qualitative features of the evolution of the squeezed state wavepacket, which is followed by the analysis of the relative fluctuations in the volume observable $\hat{V}|_\phi$ using the triangle inequalities (eqs.(2.16) and (2.20)). The key results of this analysis are: (i) the confirmation of the validity of the triangle inequality (2.16) derived in Ref. [24] for states with arbitrary parameters and (ii) finding the range of validity of a stronger version of inequalities (2.20) derived in Ref. [25] with assumptions on the semi-classicality of the initial state. We also study the behavior of the energy density at the bounce as the imaginary part of η is varied while keeping the real part fixed and compare our results with the analytical results obtained in Ref. [25] using sLQC [22]. After that, we illustrate the dynamical trajectories for various parameters by studying the behavior of the expectation value of the physical observables with respect to the internal time and compare them with the corresponding effective trajectories obtained from the effective Hamiltonian in Ref. [28]. Since the derivation of the effective Hamiltonian assumes Gaussian states we find significant departures between the quantum evolution and the effective trajectory (Sec. II C).

1. Evolution

At a qualitative level, the evolution of all states constructed using (3.5) is very similar. They all undergo a quantum bounce. However, depending on the values of η_r and η_i , the evolution of the initial states demonstrate rich distinct features. In particular, the profile of the state and dispersions can vary significantly during evolution for different initial states. Larger values of field momentum leads to larger bounce volumes and lower bounce densities. To demonstrate the way the choice of squeezedness parameters effect the properties of the state during quantum evolution we discuss three representative cases: (i) a sharply peaked initial state with $n = 0$, $\omega^* = 1000\sqrt{G}$, $\eta = (1 + i) \times 10^{-4}$, (ii) a very widely spread initial state with $n = 0$, $\omega^* = 1000\sqrt{G}$, $\eta = (1 + 10i) \times 10^{-4}$, and (iii) a sharply peaked initial state with $n = 50$, $\omega^* = 1000\sqrt{G}$, $\eta = (1 + i) \times 10^{-4}$. In the latter case, $\langle \hat{p}_\phi \rangle \neq \omega^* \hbar$ unlike the first two cases. These three cases are also summarized in Table I.

Results from the quantum evolution of case (i) are presented in Fig. 1. The evolution of $|\Psi|$ with respect to volume and time ϕ is shown in Fig. 1(a). Fig. 1(b) shows snapshots of $|\Psi|$ at different times around the bounce time ϕ_b . Note that, in all 3D figures and figures showing snapshots of the state, we do not include the whole computational domain, but rather only show the region relevant for the bounce. It is evident from these figures that the wavefunction is peaked on a non-zero finite value of the spatial volume during the entire evolution. This feature is more apparent in the projection of the amplitude of the wavefunction in the $V - \phi$ plane in Fig. 1(a). From the plot corresponding to $\phi = \phi_b$ in Fig. 1(b), we also find that the amplitude of the wavefunction decays rapidly for $V < V_b$ (shown by the dotted blue vertical curve). This decay is almost exponential, in agreement with the earlier results on the decay of the eigenfunctions in this model [3, 4] and in sLQC [38]. In the same plot we also show, via a dashed red vertical line, the estimation of the cutoff volume V_c obtained by replacing ω with the peak value ω^* (which in this case equals $\langle \hat{p}_\phi \rangle$) in eq. (3.4). Note that for this initial state V_c is almost identical to the bounce volume, since the state is sharply peaked at the bounce. The expectation value of the volume are plotted against ϕ in Fig. 1(c) and a comparison is made with the classical trajectories. As expected from the evolution of the wavefunction, the expectation value of the volume always remains non-zero. Since the initial data is provided when the spatial curvature is very small, the LQC trajectory coincides with the classical theory in the region far from the bounce. Under the backward evolution, the wavepacket travels inwards and the expectation value of the volume decreases. This in turn leads to an increment in the spacetime curvature. Quantum geometric effects become prominent when the spacetime curvature approaches Planck scale, which in turn leads to a notable difference between the LQC and classical trajectories. The LQC trajectory undergoes a non-singular bounce while the classical trajectory corresponding to the expanding solution encounters a big-bang singularity in the past evolution. In the subsequent evolution, the expectation values of the volume observable in LQC turn out to be in excellent agreement with the contracting classical solution (for the same value of field momentum) when spacetime curvature becomes much smaller than the Planck scale. The disjoint classical trajectories hence get connected by a smooth non-singular quantum gravitational bridge in LQC. Although the shape of the wavefunction before and after the bounce is similar, the spread of the state, shown in Fig. 1(d), is not symmetric. The asymmetry is also apparent in Fig. 1(b). This feature is in contrast with the behavior of the spread of a Gaussian counterpart ($\eta_i = 0$) of the squeezed state [30].

Case (ii), a very widely spread squeezed state with parameters $\omega^* = 1000\sqrt{G}$, $n = 0$ and $\eta = (1 + 10i) \times 10^{-4}$ is shown in Fig. 2. It is noteworthy that the shape of the state in Fig. 2(a) is quite different from that in Fig. 1(a), even far from the bounce. Moreover, in the vicinity of the bounce the shape of the wavefunction has prominent non-Gaussian features (see also Fig. 2(b)). It is noticeable, however, that despite the non-trivial features close to the bounce, the original shape of the wavefunction is recovered on the other side of the bounce. That is, the profile of the wavefunction on both sides of the bounce (at early and late times) is similar. Such non-Gaussian features are also seen in the simulation of very widely spread Gaussian states, as shown in Fig. 10 of Ref. [31]. It is worth mentioning

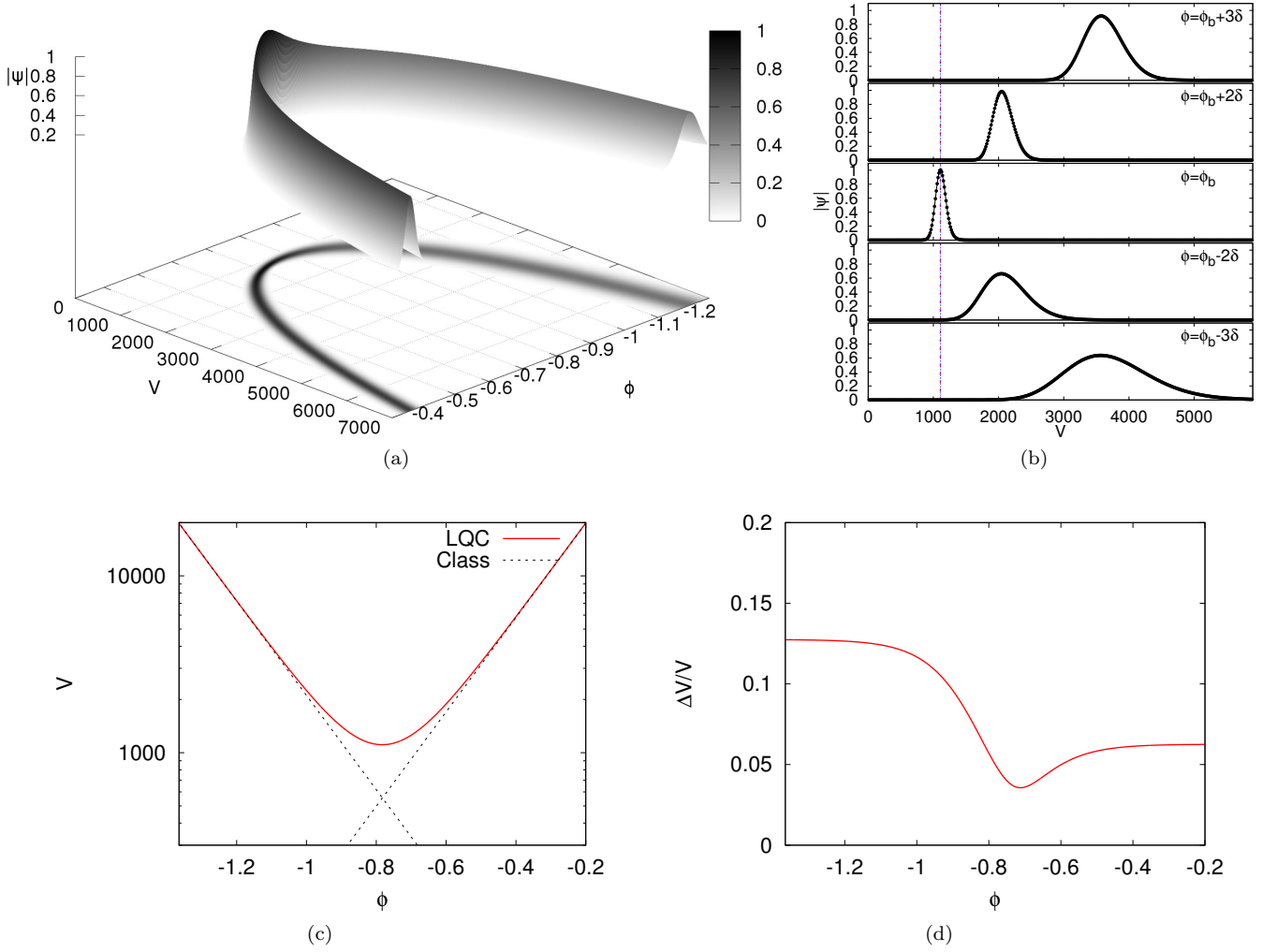


FIG. 1. Evolution of a squeezed state with $n = 0$, $\eta = (1 + i) \times 10^{-4}$ and $\omega^* = 1000 \sqrt{G}$. Panel (a) shows the amplitude of the wavefunction, $|\Psi|$, as a function of the volume V and the internal time ϕ , including a projection onto the $V - \phi$ plane to help visualizing the 3D graph. Panel (b) shows $|\Psi|$ at different values of ϕ around the bounce time, $\phi_b = -0.7830$, where $\delta = 0.1$. Note that the wavefunction has support only on the discrete lattice, but for a better visualization we use continuous curves for the snapshots of $|\Psi|$ in this and the following figures. The blue dotted line indicates the bounce volume, $V_b = 1109.3 V_{P1}$, and the red dashed one indicates the cutoff volume, $V_c = 1105.7 V_{P1}$ estimated from sLQC. In this case the values are so close that one cannot easily distinguish the two vertical curves in the figure. Panel (c) presents a comparison between the LQC and classical GR trajectories. Panel (d) shows the relative dispersion $\Delta V/V$. All values are given in Planck units, and we have chosen the notation $V = \langle \hat{V} | \phi \rangle$ and $\Delta V = \langle \Delta \hat{V} | \phi \rangle$ in the trajectory figures. The same convention is used in all the figures in this paper.

here that the non-Gaussian features observed in the case of widely spread states is a phenomena which was not seen in the early numerical simulations of [3, 4] as they were limited to sharply peaked states only. Also, these features are *not* artifacts of numerical techniques as confirmed by several robustness tests of these simulations. It is apparent from these figures that, despite some small differences in the evolution in the high curvature regime, squeezed states also undergo a smooth quantum bounce. Unlike case (i), since this squeezed state has more significant quantum features at the bounce time, the bounce volume (V_b) computed from the expectation value of volume observable and the cutoff volume (V_c) are significantly different. For this reason, the almost exponential decay of $|\Psi|$ does not occur below V_b , but occurs below V_c as is evident from the plot for $\phi = \phi_b$.

Finally, figures 3(a) and 3(b) show the evolution of the squeezed state with parameters $\omega^* = 1000 \sqrt{G}$, $n = 50$ and $\eta = (1 + i) \times 10^{-4}$ (case (iii)). As in the cases with $n = 0$, the state is always peaked on a non-zero finite volume, while undergoing a non-singular bounce. Further, as expected, the expectation value of the field momentum remains constant throughout the evolution. Note that, even though cases (i) and (iii) correspond to the same value

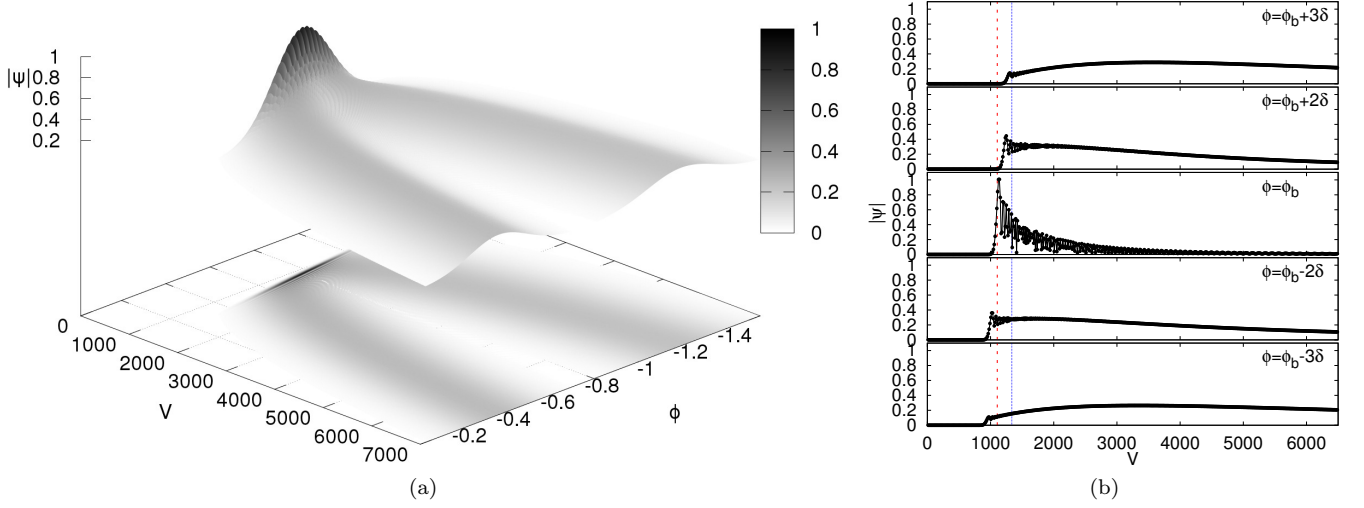


FIG. 2. Evolution of a squeezed state with $n = 0$, $\eta = (1 + 10i) \times 10^{-4}$ and $\omega^* = 1000 \sqrt{G}$. Panel (a): $|\Psi|$, including the projection onto the V - ϕ plane to help visualize the 3D plot. Panel (b): $|\Psi|$ at different values of ϕ close to the bounce, as indicated in the figure, where $\phi_b = -0.7785$ and $\delta = 0.1$. The blue dotted line indicates the bounce volume, $V_b = 1336.3 V_{P1}$, and the red dashed one indicates the cutoff volume, $V_c = 1105.7 V_{P1}$.

of $\omega^* = 1000 \sqrt{G}$, the expectation value of the field momentum for $n = 0$ is $\langle \hat{p}_\phi \rangle = 1000 \sqrt{G} \hbar$, while for $n = 50$ it is $\langle \hat{p}_\phi \rangle = 1207 \sqrt{G} \hbar$. If one naively computes the cutoff volume for this state using $\omega = \omega^*$, one underestimates the volume below which the almost exponential decay of the amplitude of wavefunction occurs to be $V_c \approx 1106 V_{P1}$. Instead, if we estimate the cutoff volume V_c by using $\omega = \langle \hat{p}_\phi \rangle / \hbar$ in eq. (3.4), we find that this provides the correct volume below which $|\Psi|$ decays almost exponentially. Similarly to case (i), the bounce volume and the cutoff volume are approximately the same in this case.

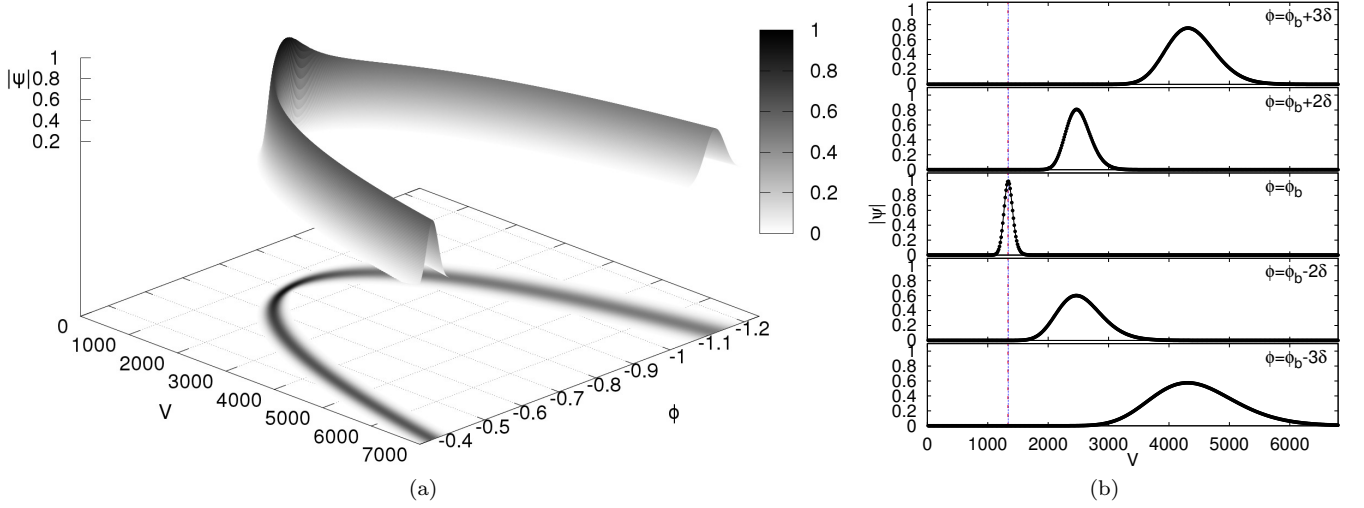


FIG. 3. Evolution of a squeezed state with $n = 50$, $\eta = (1 + i) \times 10^{-4}$ and $\omega^* = 1000 \sqrt{G}$. The expectation value of the field momentum is $\langle \hat{p}_\phi \rangle = 1207 \sqrt{G} \hbar$. Panel (a): $|\Psi|$, including the projection onto the V - ϕ plane. Panel (b): $|\Psi|$ at different values of ϕ close to the bounce, as indicated in each sub-figure, where $\phi_b = -0.7417$ and $\delta = 0.1$. The blue dotted line indicates the bounce volume, $V_b = 1339.4 V_{P1}$, and the red dashed curve indicates the cutoff volume, $V_c = 1334.6 V_{P1}$. Note that the values are so close that the two lines are indistinguishable from each other.

2. Dispersions and triangle inequalities

Let us now discuss the behavior of the dispersion of the state as a function of the internal time. The relation between the dispersions on the two sides of the bounce in the presence of a massless scalar field has been analytically understood in Ref. [24], where it was shown that the relative fluctuations in the field momentum and the volume observable follow triangle inequalities which constrain the growth of the dispersion of the state during the evolution. As discussed in Sec. II B, a stronger form of the triangle inequality (2.20) can be derived for states which satisfy $\langle \Delta \ln(\hat{\mathcal{O}}) \rangle \approx \langle \Delta \hat{\mathcal{O}} \rangle / \langle \hat{\mathcal{O}} \rangle$. Here, we will study how the relative dispersions in the volume observable and in the momentum of the matter field change across the bounce and the validity of triangle inequalities (2.16) and (2.20).

As an example, let us consider different squeezed states with $n = 0$, $\eta_r = 1 \times 10^{-4}$, $\omega^* = 1000\sqrt{G}$. The evolution of $\Delta V/V$ for such states are shown in Fig. 4 for various values of η_i . Compared to their Gaussian counterparts, squeezed states show some similarities and some important differences. The solid (red) curve in Fig. 4 shows $\Delta V/V$ for $\eta_i = 0$, that is a pure Gaussian, for which the relative volume dispersion takes the same value on either side of the bounce. On the other hand, it is evident from the figure that for $\eta_i \neq 0$, the asymptotic values of $\Delta V/V$ on the two sides of the bounce are different. Moreover, it shows a mirror symmetry with respect to the bounce point for opposite signs of η_i for a fixed η_r . That is, the plot of $\Delta V/V$ for η_i is a mirror image of the one for $-\eta_i$, with the center of the mirror being the bounce point. As mentioned in Sec. III A, the initial data is constructed with a phase factor $e^{-i\alpha}$ (which corresponds to method-3 of Refs. [3, 30]). Due to this phase factor, the relative dispersion in volume of the corresponding Gaussian state has a symmetric behavior, and the eigenfunctions of the evolution operator in Wheeler-DeWitt theory match those in LQC. If the phase factor is not included in the initial data, the above mirror symmetry will not be present. We also find that all pairs of mirror symmetric curves intersect at the bounce.

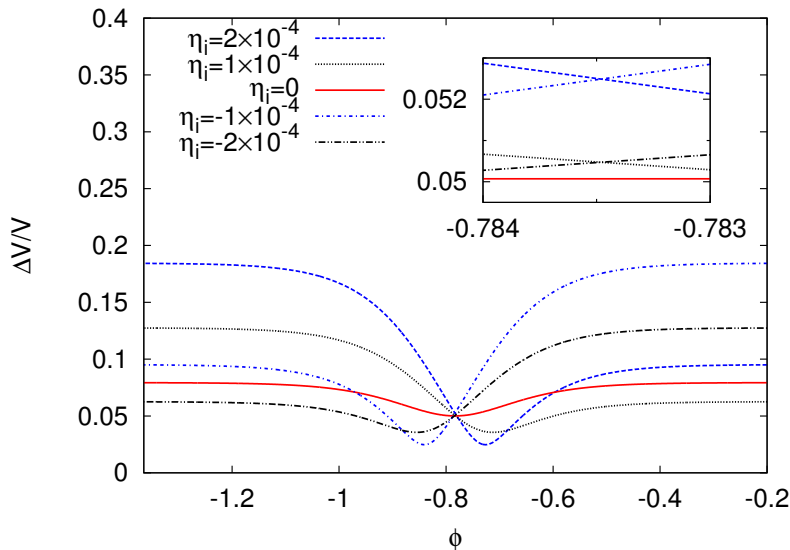


FIG. 4. Relative volume dispersion for various values of η_i and fixed $\eta_r = 1 \times 10^{-4}$ are shown. The expectation value of the field momentum for all curves is $\langle \hat{p}_\phi \rangle = 1000\sqrt{G}\hbar$ and $\omega^* = 1000\sqrt{G}$. It is evident that all curves intersect each other at the same value of ϕ , and the curves corresponding to η_i are mirror images of those with $-\eta_i$.

It was shown analytically in Ref. [24] that, irrespective of the particular state, the dispersions $\Delta \ln(V)$ and $\Delta \ln p_\phi$ for a flat FRW model in the presence of a massless scalar field obey the inequality given in eq. (2.16). For the sharply peaked Gaussian states, the dispersion in an observable $\ln(\hat{\mathcal{O}})$ can be approximated by $\langle \Delta \ln(\hat{\mathcal{O}}) \rangle \approx \langle \Delta \hat{\mathcal{O}} \rangle / \langle \hat{\mathcal{O}} \rangle$, which for the simplicity of the notation is denoted by $\Delta \mathcal{O} / \mathcal{O}$ in the rest of the paper. Based on this approximation the triangle inequalities can be expressed in terms of the quantity \mathcal{E} as described in eq. (2.20), where \mathcal{E} remains smaller than unity in the regime where the above approximation is valid. Whether or not this inequality holds is determined by the squeezedness of the state, as is shown below.

Fig. 5(a) shows the difference between the asymptotic values of the dispersions σ_\pm (computed from (2.16)) on the two sides of the bounce compared with 2σ for $\omega^* = 1000\sqrt{G}$ and two values of η_r with varying η_i . The red (light) curve in the figure corresponds to $\eta_r = 1 \times 10^{-4}$ and the black (dark) one to $\eta_r = 5 \times 10^{-5}$. This figure shows clearly that the difference between the asymptotic values of the dispersions σ_\pm on the two sides of the bounce is always less than 2σ . That is, the triangle inequality in eq. (2.16) remains valid for all the states considered. Fig. 5(b), on the

other hand, shows the variation of \mathcal{E} with varying $|\eta_i|$. It is apparent that \mathcal{E} is smaller than unity for small $|\eta_i|$. As $|\eta_i|$ increases, \mathcal{E} also increases. As a result \mathcal{E} becomes greater than unity for some value of $|\eta_i|$ (dependent on η_r), hence violating the inequality in eq. (2.20) for large η_i .

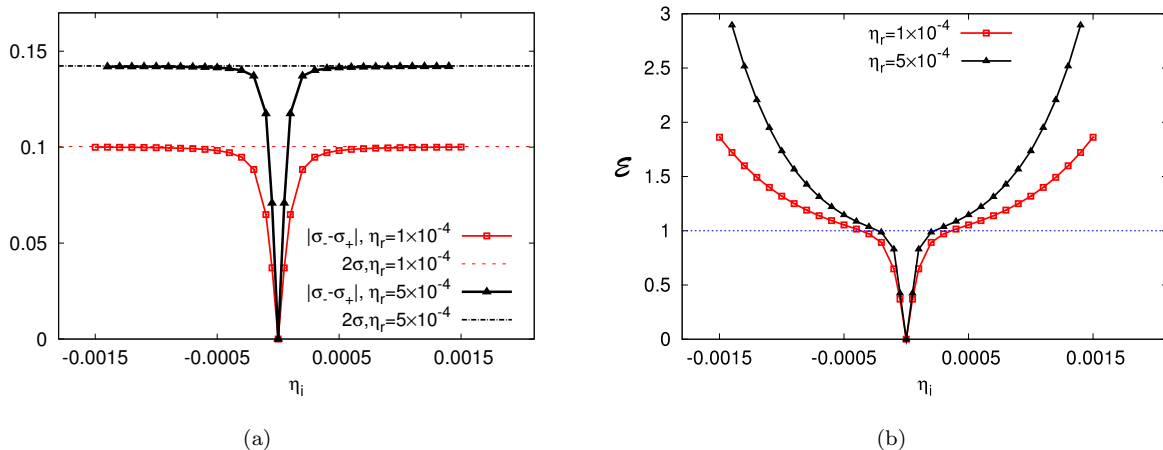


FIG. 5. Panel (a) demonstrates the validity of the triangle inequality as described by eq. (2.16) for the $n = 0$ squeezed states. Panel (b) shows the violation of the triangle inequality (2.20) derived for semi-classical states, and the variation of \mathcal{E} with varying η_i . \mathcal{E} remains smaller than 1 as long as $|\eta_i|$ is close to zero. The two curves correspond to: $\eta_r = (1 \times 10^{-4}, 5 \times 10^{-5})$ and $\omega^* = 1000 \sqrt{G}$.

3. Energy density

As discussed previously, numerical simulations for sharply peaked Gaussian states show that the quantum bounce occurs close to the maximum value the matter energy density in sLQC, given by $\rho_{\max} \approx 0.409 \rho_{\text{Pl}}$ [4, 30]. For widely spread Gaussian states, however, ρ_b can be significantly smaller than ρ_{\max} [30]. On the other hand, the energy density at the bounce in the effective description of a flat FRW model is always equal to its absolute upper bound, i.e. $\rho_b^{\text{eff}} = \rho_{\max}$. Thus, the effective theory always overestimates the energy density at the bounce for the Gaussian initial states [30]. We see the same qualitative behavior of ρ_b to hold for squeezed states.

We computed the energy density at the bounce for various squeezed states and found that it varies monotonically with $|\eta_i|$, always remaining below ρ_{\max} and reaching its maximum value for $\eta_i = 0$. The variation of the energy density at the bounce for squeezed states was studied analytically in the context of the exactly solvable model in Ref. [26]. Fig. 6 shows the values of the energy density at the bounce for two values of η_r and varying η_i . The solid (black) curves show the bounce energy density obtained via analytical calculation following Ref. [26], while the (red) symbols correspond to the bounce density computed from the numerical simulations. The centers of the error bars show ρ_b and the error bars themselves denote the spread in the energy density. It is remarkable to see that there is an excellent agreement between the analytical predictions from sLQC and our numerical simulations even though the Hamiltonian constraint in the present analysis is different from sLQC.

4. Comparison with the effective theory

So far we have discussed the evolution of the squeezed state wavefunctions, their dispersion and the energy density at the bounce for various choices of parameters. Let us now consider the trajectories, as described by the expectation value of the volume observable as a function of the internal time. A detailed comparison of such trajectories with the corresponding effective ones for Gaussian states were performed in Ref. [30], with the conclusion that for all types of Gaussian initial data considered, the effective trajectory obtained from eq. (2.21) always underestimates the bounce volume. We obtain the same qualitative behavior for squeezed states in the numerical simulations performed in this paper.

In Fig. 7, we compare the trajectories of four different squeezed states with $n = 0$. The particular cases shown are chosen to illustrate the effects of varying one property of the initial state at a time. Specifically, Fig. 7(a) and Fig. 7(b)

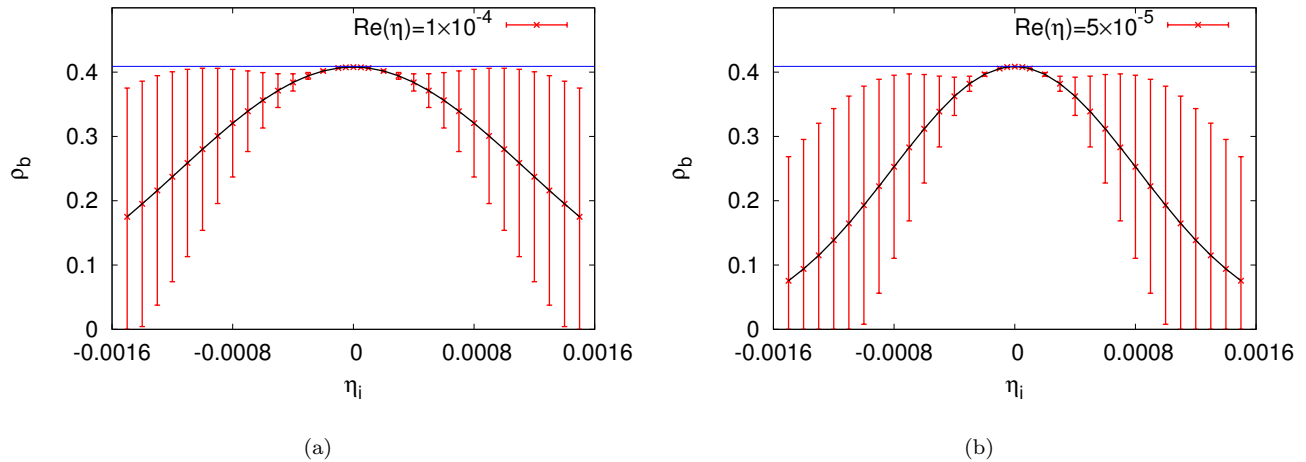


FIG. 6. The energy density at the bounce computed for various values of η_i and fixed $\eta_r = 1 \times 10^{-4}$ in Fig. 6(a) and $\eta_r = 5 \times 10^{-5}$ in Fig. 6(b). The error bars represent the spread in ρ . It is clear that the energy density at the bounce is always bounded above by $\rho_{\max} \approx 0.409\rho_{\text{Pl}}$ predicted by sLQC (shown by horizontal line), and the energy density at the bounce decreases with increased squeezing.

correspond to states that differ only in η_i , whereas Fig. 7(a) and Fig. 7(c) correspond to initial states with different η but with the same ratio η_i/η_r , all of them with the same ω^* . Finally, Fig. 7(c) and Fig. 7(d) correspond to states with different ω^* , but with the same η . The particular values of ω^* and η are indicated in each sub-figure. We see that increasing $|\eta|$, either by keeping the same ratio η_i/η_r or by increasing η_i alone, leads to a wider state, resulting in an increased deviation between the effective and the LQC trajectories close to the bounce as well as an increased bounce volume. Comparing Fig. 7(c) and Fig. 7(d) we see that decreasing ω^* , while resulting in a smaller bounce volume, may nonetheless result in a similar relative deviation from the effective theory. This is evident from the qualitative similarity between these two figures (although the scales differ by an order of magnitude).

As is customary in the literature, we represent the dispersion ΔV in the figures by means of error bars. Note, however, that for non Gaussian states the error bars may fall below $V = 0$ in some cases. This, of course, does not mean $|\Psi| > 0$ for $V \leq 0$, but is an artifact of the way error bars are defined (centered around the mean value of volume observable). In fact, as discussed earlier, the amplitude of the wavefunctions decay almost exponentially in the regime $V < V_c$, and $|\Psi|$ is zero when volume is zero.

A similar trend can also be observed for the deviation between the effective and the LQC trajectories for the squeezed states with $n = 50$. Fig. 8 shows the comparison of the effective and LQC trajectories for $\omega^* = 1000\sqrt{G}$ in panel(a) and for $\omega^* = 50\sqrt{G}$ in panel (b), both for $\eta = 3 \times 10^{-4} + 3 \times 10^{-4}i$. It is evident from these figures that in the case of $\omega^* = 1000\sqrt{G}$, where the dispersion in the state is small, there are small differences between the LQC and effective theory. These differences are much more prominent for $\omega^* = 50\sqrt{G}$, for which the states have large dispersion. Once again, the effective theory predicts a smaller bounce volume in comparison to the quantum evolution.

So far we have discussed the evolution of squeezed states for various values of the initial parameters. In all the cases discussed here, the evolutions are non-singular and undergo a quantum bounce, showing similar qualitative features as the evolution of Gaussian states. We have also seen that the numerical results regarding the variation of the energy density with respect to the imaginary part of η are in very good agreement with the analytical results obtained in Ref. [26], and the triangle inequality derived in the Ref. [24] is obeyed irrespective of the initial data considered. In the following we now study the evolution of two more non-Gaussian states, which have quite different features compared to a Gaussian state. For these states we will discuss the evolution of the wavepacket and compare the LQC trajectories with the corresponding effective one for both small and large dispersions.

B. Multi-peaked-1 states

We now discuss results from our analysis for initial states which are constructed as a sum of Gaussians in k space (eq.(3.6)). The two Gaussians are separated by the parameter δk . The initial state for the evolution is then obtained

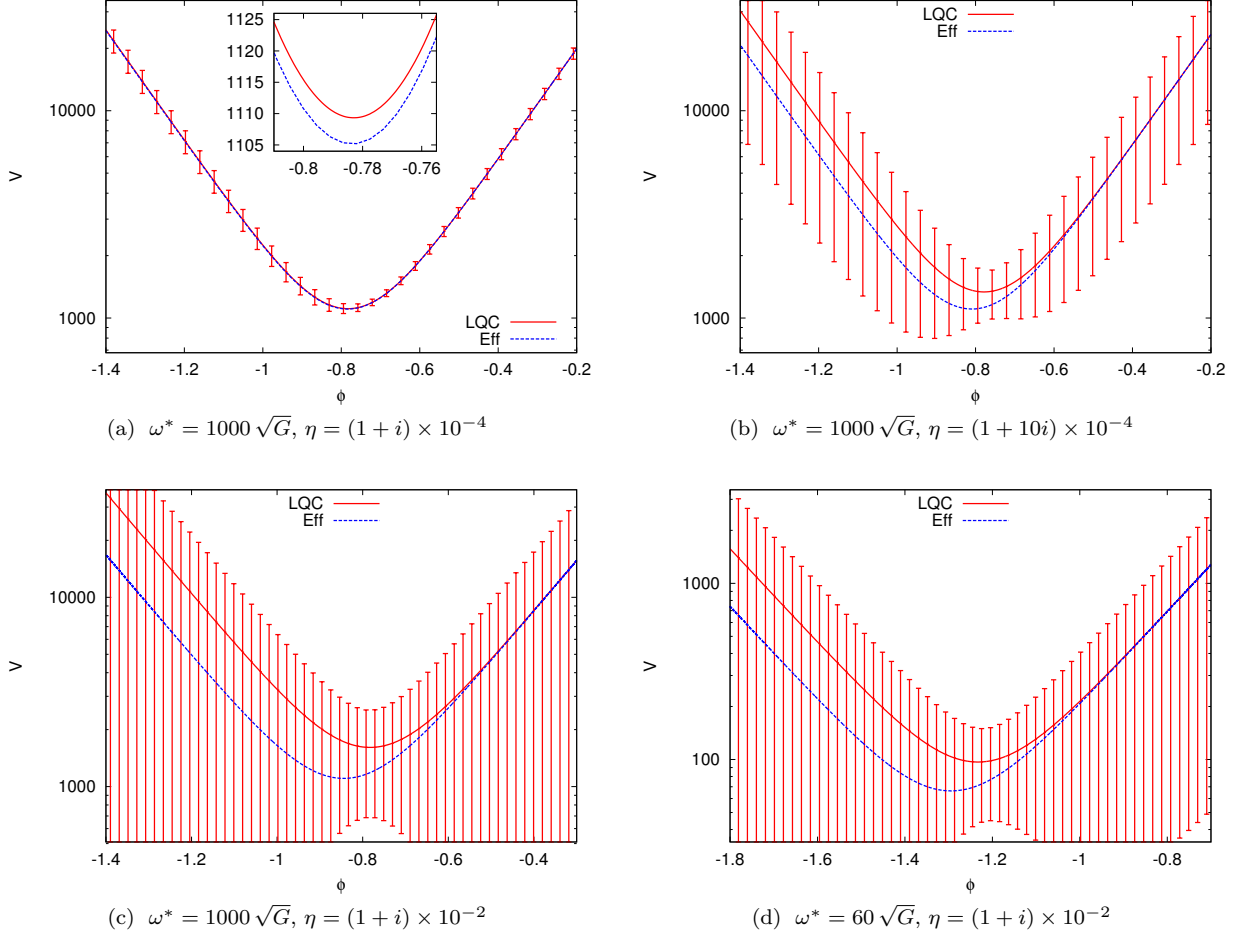


FIG. 7. Evolution trajectories for squeezed states with $n = 0$. Panel (a): $\omega^* = 1000 \sqrt{G}$ and $\eta = (1 + i) \times 10^{-4}$. Panel (b): $\omega^* = 1000 \sqrt{G}$ and $\eta = (1 + 10i) \times 10^{-4}$. Panel (c): $\omega^* = 1000 \sqrt{G}$ and $\eta = (1 + i) \times 10^{-2}$. Panel (d): $\omega^* = 60 \sqrt{G}$ and $\eta = (1 + i) \times 10^{-2}$. The solid (red) curves, with the error bars representing the dispersion, show the LQC trajectories, while the dashed (blue) curves show the corresponding effective trajectories.

by evaluating the integral that transforms the state into the volume representation. The resulting state may have several local peaks, depending on the value of the parameters. Thus, such states, unlike the squeezed states considered earlier, are therefore not peaked at any classical volume at the initial time. The state is still chosen such that the expectation value of the volume at the initial time is very large and the corresponding energy density is very small compared to the Planck density. Irrespective of the choice of parameters, we find that loop quantum evolution is non-singular for all such states and the existence of a quantum bounce is robust. Whether or not the effective trajectory obtained from (2.21) captures the underlying quantum evolution depends on the relative dispersion in volume. As long as the relative dispersion in volume is small, the effective dynamics is an excellent approximation – a remarkable result, since these states are very different from the Gaussian states used in the derivation of the effective Hamiltonian constraint [28]. For multi-peaked-1 states with a large dispersion in volume, on the other hand, we find significant deviations between the effective and LQC trajectories. As with the squeezed states with large dispersions, the energy density at the bounce is much smaller than the universal maximum ρ_{\max} in sLQC.

As a representative case of simulations of multi-peaked-1 states, Fig. 9 shows the evolution of a state with $\omega^* = 1000 \sqrt{G}$, $\eta = 2 \times 10^{-4}$ and $\delta k = 2$. Fig. 9(a) shows the 3D evolution of the wavefunction plotted against the volume V and the emergent time ϕ . Fig. 9(b) shows snapshots of the wavefunction around the bounce time ϕ_b . That the shape of the wavepacket is highly non-Gaussian is seen most clearly in Fig. 9(b). During the entire evolution, the state has support on non-zero finite volume and undergoes a non-singular bounce. Note that in this case since the state has no well defined single peak, it is not possible to single out a value of ω at which the state may be considered peaked and therefore it is not possible to evaluate the cutoff volume using eq.(3.4). Another interesting feature of the evolution

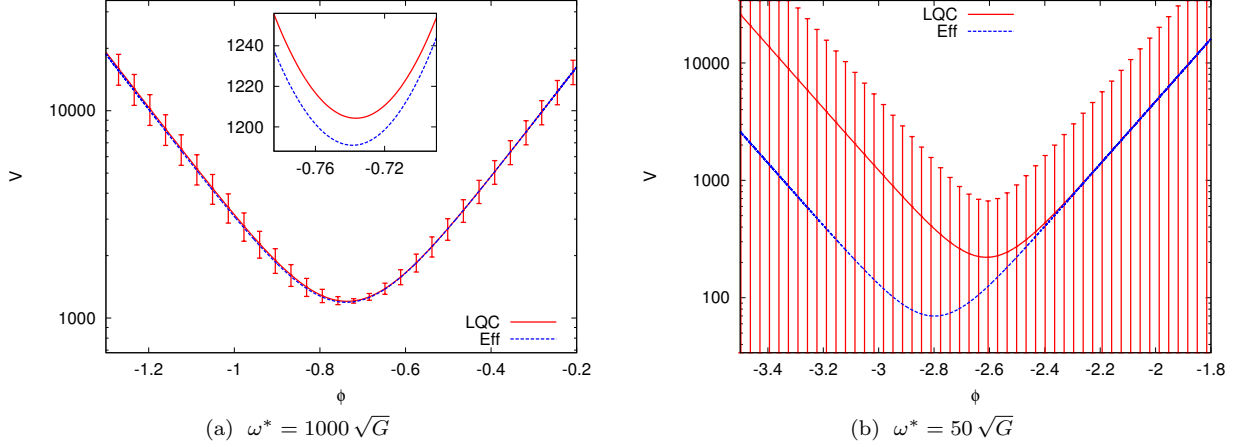


FIG. 8. Expectation value of V as a function of the emergent time ϕ for squeezed states with $n = 50$, $\eta = 3 \times 10^{-4} + 3 \times 10^{-4}i$ and different values of ω^* , indicated in each panel. The solid (red) curves, with the error bars representing the dispersion, show the LQC trajectories, while the dashed (blue) curves show the corresponding effective trajectories. There is an excellent agreement between the two trajectories for $\omega^* = 1000\sqrt{G}$ (panel (a)), whereas the differences are prominent for $\omega^* = 50\sqrt{G}$ (panel (b)).

is that the shape of the wavepacket is recovered on the other side of the bounce. For example, at $\phi_b + 3\delta$ and $\phi_b - 3\delta$ the amplitude of the wavefunction has almost the same profile, as shown in the first and the last panel of Fig. 9(b).

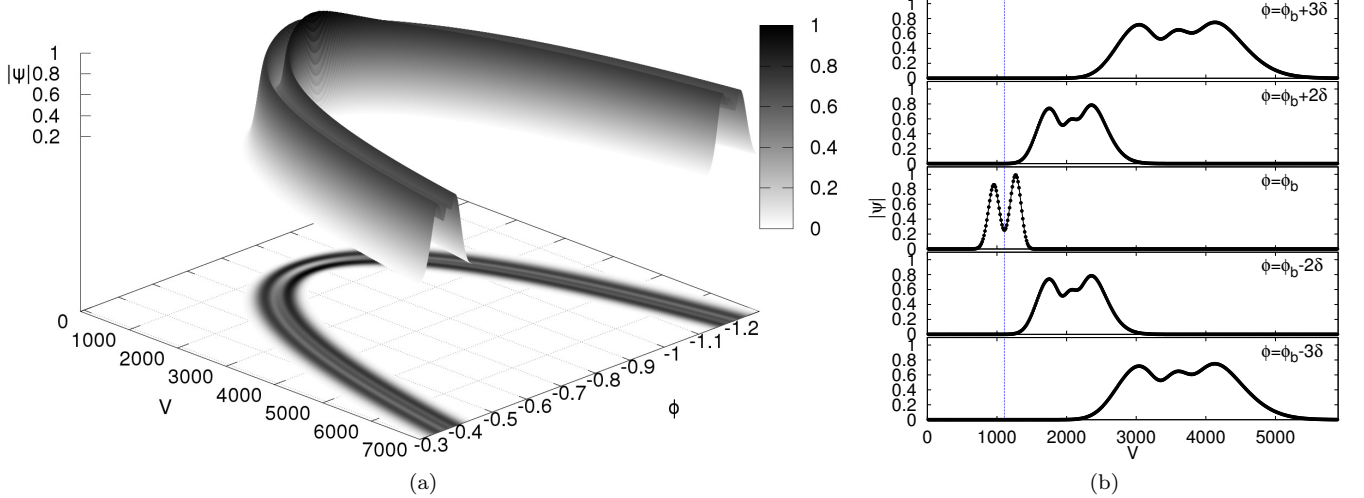


FIG. 9. Evolution of a multip peaked-1 initial state with $\omega^* = 1000\sqrt{G}$, $\eta = 2 \times 10^{-4}$ and $\delta k = 2$. Panel (a): $|\Psi|$, including the projection onto the V - ϕ plane, shown to help visualizing the 3D graph. Panel (b): $|\Psi|$ at different values of ϕ around the bounce time, $\phi_b = -0.7835$, as indicated, where $\delta = 0.1$. The blue dotted line indicates the bounce volume $V_b = 1108.7 V_{P1}$.

In figure 10 we present results for another multip peaked-1 state, with $\eta = 2 \times 10^{-2}$, $\omega^* = 50\sqrt{G}$ and $\delta k = 2$. This state has a quite different profile and a much larger spread, showing features at small volume that are similar to those in case (ii) of the squeezed states presented in Sec. IVA (see Fig. 2 for a comparison), which also had a very large spread. Despite being highly quantum in nature, with a very large spread, the shape of the wavefunction is preserved through the non singular bounce. We will see, however, that in this case the trajectory obtained from the effective Hamiltonian deviates significantly more than the case discussed in Fig. 9.

Fig. 11 shows the comparison of the LQC and the corresponding effective trajectory for the multip peaked-1 states presented in this subsection. For the state with $\omega^* = 1000\sqrt{G}$ and $\eta = 2 \times 10^{-4}$, shown in Fig. 11(a), the relative volume dispersion of the initial state is small: $\Delta V/V = 0.13$ and the bounce happens at $V_b \approx 1109 V_{P1}$. This results in quite good agreement between the two trajectories. On the other hand, for the state with $\omega^* = 50\sqrt{G}$

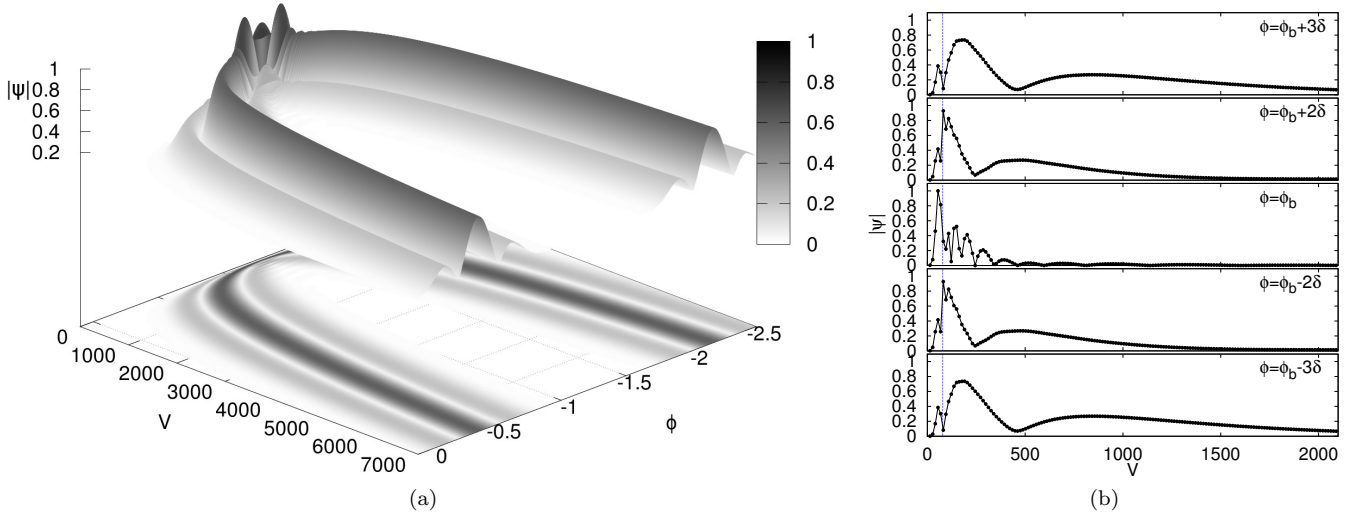


FIG. 10. Evolution of an multi-peaked-1 initial state with $\omega^* = 50\sqrt{G}$, $\eta = 2 \times 10^{-2}$ and $\delta k = 2$. Panel (a): $|\Psi|$, including the projection onto the V - ϕ plane. Panel (b): $|\Psi|$ at different values of ϕ close to the bounce time, $\phi_b = -1.271$, as indicated in the figure, where $\delta = 0.1$. The blue dotted line indicates the bounce volume, $V_b = 78.231 V_{P1}$.

and $\eta = 2 \times 10^{-2}$, shown in Fig.11(b), the initial dispersion in volume is $\Delta V/V = 1.16$ and $V_b \approx 78.23 V_{P1}$ and consequently there is a significant difference between the effective and the corresponding LQC trajectory. It is also worth noticing that the energy density at the bounce ρ_b satisfies the upper bound limit in both cases. Similarly to the case of squeezed states, ρ_b is closer to the absolute maximum ρ_{\max} for smaller $\Delta V/V$ in these simulations.

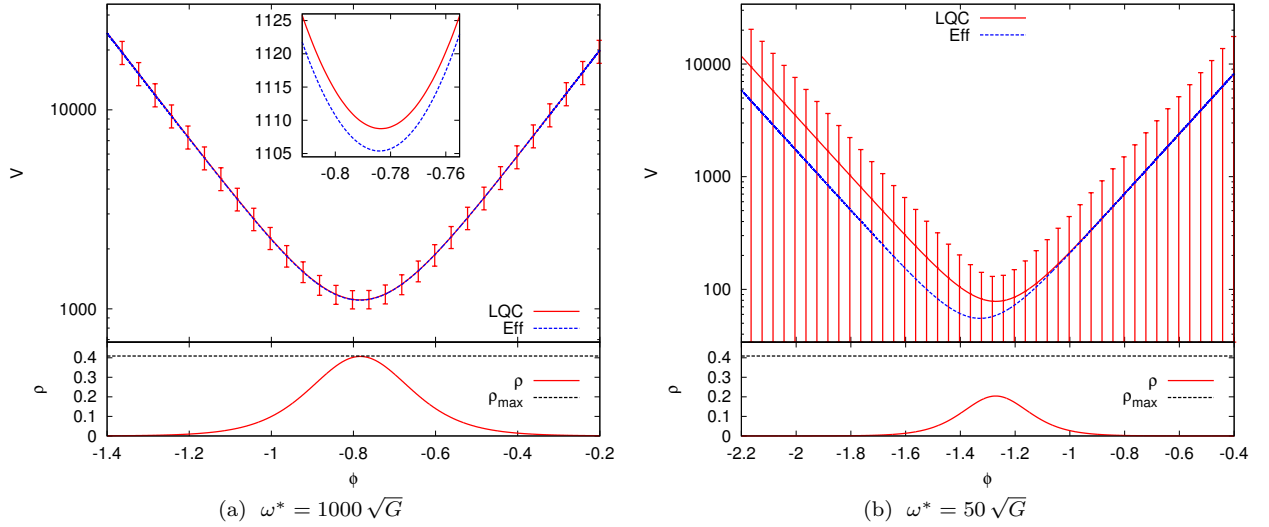


FIG. 11. Comparison of the LQC and effective trajectories and evolution of energy densities for a multi-peaked-1 state with $\omega^* = 1000\sqrt{G}$ and $\eta = 2 \times 10^{-4}$ (panel (a)) and for $\omega^* = 50\sqrt{G}$ and $\eta = 2 \times 10^{-2}$ (panel (b)). In both cases $\delta k = 2$. The solid (red) curve, with the error bars showing the dispersion in volume, corresponds to the LQC trajectory and the dashed (blue) curve shows the corresponding effective trajectory. For large ω^* the relative volume dispersion is small and the effective theory is in good agreement with the LQC one, whereas $\Delta V/V$ is large for small ω^* and the difference between the LQC and the effective theory is more prominent. We see that for the multi-peaked-1 state with the larger fluctuation the energy density at the bounce is only half of the maximum value of the energy density (ρ_{\max}) predicted in sLQC.

Let us now examine the validity of the triangle inequalities. Fig.12 shows the dispersion $\Delta \ln(\widehat{V})$ and the quantity $\sigma_{\pm} + 2\sigma$ (computed using (2.17)), plotted for $\omega^* = 1000\sqrt{G}$ and $\omega^* = 50\sqrt{G}$. In this figure 2σ is a constant of motion and the asymptotic values of the volume dispersions on both sides of the bounce are the same. Therefore, the horizontal curves for $\sigma_+ + 2\sigma$ and $\sigma_- + 2\sigma$ overlap. It is apparent from the figure that $\sigma_{\pm} + 2\sigma$ remains larger than

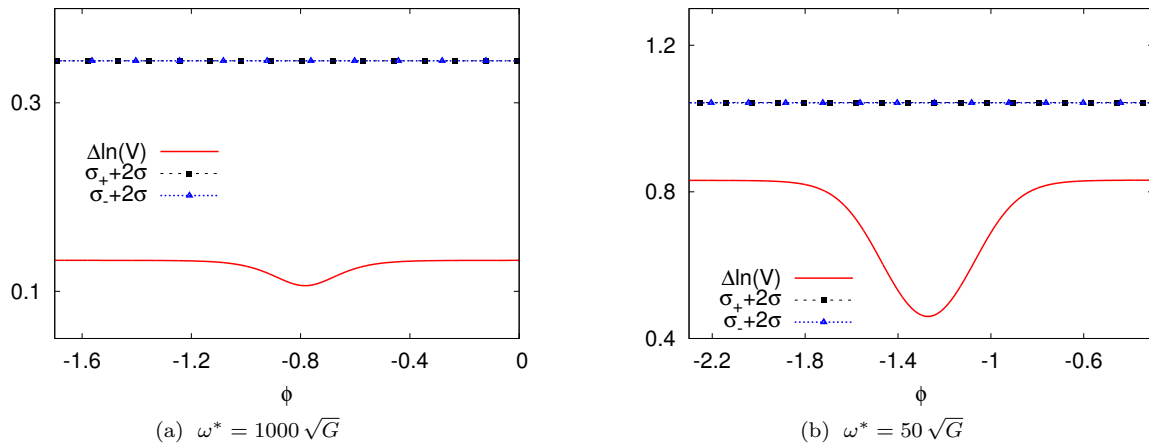


FIG. 12. The triangle inequality is shown to be valid for multi-peaked-1 states with $\omega^* = 1000\sqrt{G}$ and $\eta = 2 \times 10^{-4}$ (panel(a)); and with $\omega^* = 50\sqrt{G}$ and $\eta = 2 \times 10^{-2}$ (panel(b)). In both cases $\delta k = 2$. It is evident that $\sigma_{\pm} + 2\sigma$ (shown by horizontal curves) remains greater than $\Delta \ln(\hat{V})$ (shown by solid red curve) throughout the evolution. Since, σ remains constant throughout the evolution and the volume dispersions on both sides are practically the same in both cases, the horizontal curves for $\sigma_+ + 2\sigma$ and $\sigma_- + 2\sigma$ overlap.

TABLE II. Relative dispersion in the field momentum (Σ) and the asymptotic relative volume dispersions (Σ_{\pm}) for multi-peaked-1 and 2 states used to evaluate the triangle inequality given in eq. (2.20). This inequality ($\mathcal{E} < 1$) is satisfied in all cases considered.

ω^*	η	Σ_+	Σ_-	Σ	\mathcal{E}
Multi-peaked-1					
1000	0.0002	0.132983	0.132982	0.1052	0.000005
50	0.02	1.15910	1.15813	0.2104	0.002068
Multi-peaked-2					
1000	0.0001	0.221726	0.221724	0.1388	0.000007
200	0.0025	1.17373	1.17376	0.1389	0.000108

$\Delta \ln(\hat{V})$ throughout the evolution, which implies that the triangle inequality given in eq. (2.16) is satisfied. A similar analysis shows that the triangle inequality in eq. (2.20) is satisfied both for the case $\omega^* = 1000\sqrt{G}$ and $\omega^* = 50\sqrt{G}$. Note that for both of these cases, the state is not sharply peaked. In fact, for the case $\omega^* = 50\sqrt{G}$ the state is highly quantum. Yet, the stronger form of triangle inequality (2.20) is satisfied. The reason for this lies in the fact that the underlying construction of states is based on “method-3” in Refs. [4, 30] (see eq.(3.2)) due to which the difference in relative fluctuations in volume at large $|\phi|$ much earlier and after the bounce remains much smaller than unity for the values of parameters considered for these multi-peaked-1 states (Table II). This is the primary reason why states, which have little in common with sharply peaked states (in particular the one with $\omega^* = 50\sqrt{G}$), satisfy the stronger triangle inequality.¹³ This observation suggests that it is difficult to associate (2.20) with the semi-classicality of the state. As we see here, it is possible to construct highly quantum states which satisfy the inequality (2.20).

C. Multi-peaked-2 states

In order to probe the robustness of the quantum bounce even further, we consider yet another type of initial state with a non-Gaussian waveform. We call these multi-peaked-2 states, which in comparison to multi-peaked-1 states have many more peaks and are highly non-Gaussian. We show the wavefunction evolution for two cases of multi-peaked-2

¹³ It can be expected that if the same initial state was constructed in a different way, say by using “method-2” of Ref. [4, 30], where Wheeler-DeWitt eigenfunctions are not multiplied by a phase factor $e^{-i\alpha}$ as in “method-3” or the parameter η was chosen to be complex as in the case of squeezed states, the inequality (2.20) may not be satisfied.

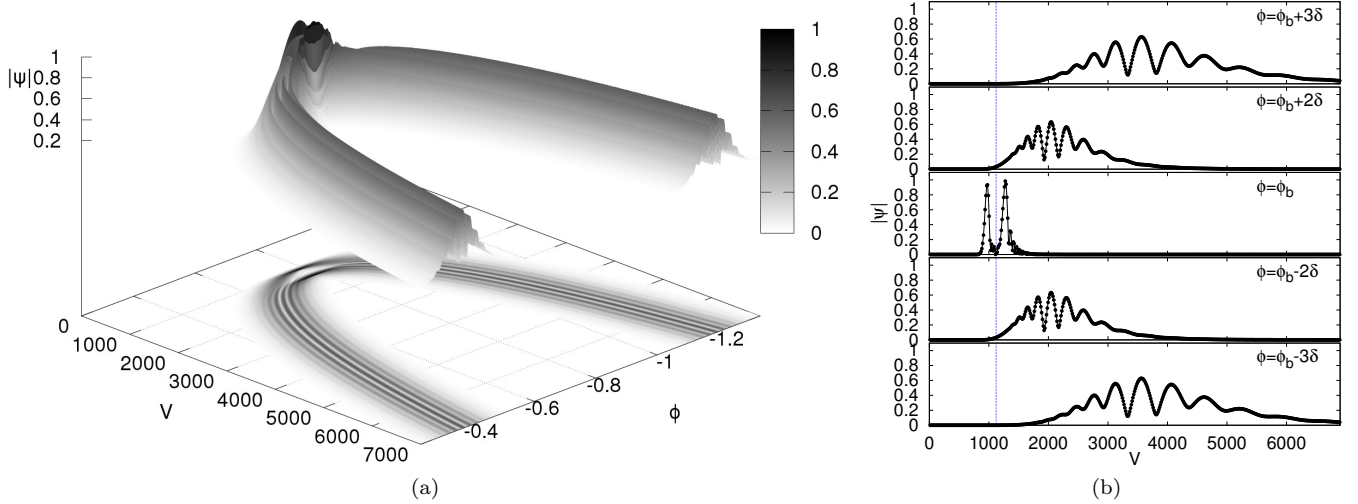


FIG. 13. Evolution of a multip peaked-2 state with $\omega^* = 1000\sqrt{G}$, $\eta = 10^{-4}$ and $\delta k = 2$. Panel (a): $|\Psi|$ including the projection onto the $V - \phi$ plane. Panel (b): $|\Psi|$ at different values of ϕ close to the bounce, as indicated in the figure, where $\phi_b = -0.7835$ and $\delta = 0.1$. The blue dotted line indicates the bounce volume, $V_b = 1121.1 V_{P1}$.

states, one with large and one with small ω^* : Figure 13 corresponds to $\omega^* = 1000\sqrt{G}$ and $\eta = 10^{-4}$ and Figure 14 corresponds to $\omega^* = 200\sqrt{G}$ and $\eta = 2.5 \times 10^{-3}$. In both cases $\delta k = 2$. The initial data is chosen so that the energy density is much smaller than the Planck density and the expectation value of the volume variable is very large compared to the Planck volume. It is evident that, despite the highly non-Gaussian features of the initial state, the wavefunction undergoes a non-singular evolution and a quantum bounce takes place. It is noteworthy that, like in the case of the Gaussian states, the shape of the wavepacket remains the same on the two sides of the bounce, although the behavior in the vicinity of the bounce is quite different from the initial state. This behavior is more noticeable in the smaller ω^* case, for which the bounce occurs at smaller volume.

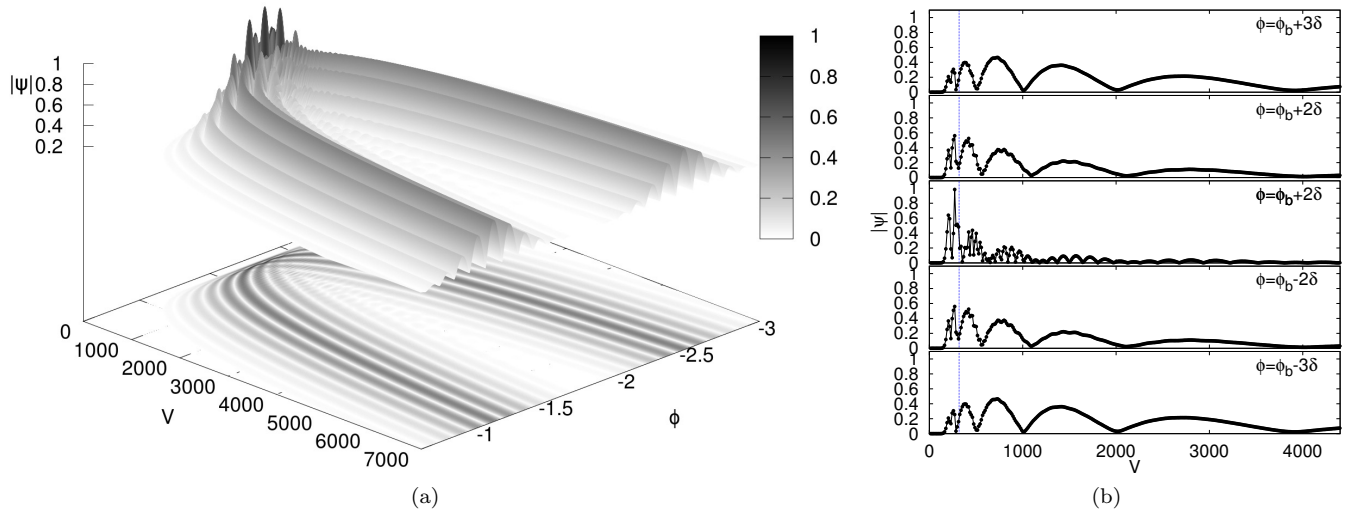


FIG. 14. Evolution of a multip peaked-2 state with $\omega^* = 200\sqrt{G}$, $\eta = 2.5 \times 10^{-3}$ and $\delta k = 2$. Panel (a): $|\Psi|$ including the projection onto the $V - \phi$ plane. Panel (b): $|\Psi|$ at different values of ϕ close to the bounce, as indicated in the figure, where $\phi_b = -1.796$ and $\delta = 0.1$. The blue dotted line indicates the bounce volume, $V_b = 318.85 V_{P1}$.

Let us now compare the trajectories of multi-peaked states in LQC with those of the effective theory. Fig. 15 shows the expectation value of the volume variable as a function of ϕ for both LQC and the effective theory. In the first case, shown in Fig. 15(a), the initial volume dispersion is small ($\Delta V/V = 0.22$) and the effective theory is a good approximation to the full LQC trajectory. On the other hand, in the second case the initial volume dispersion is large

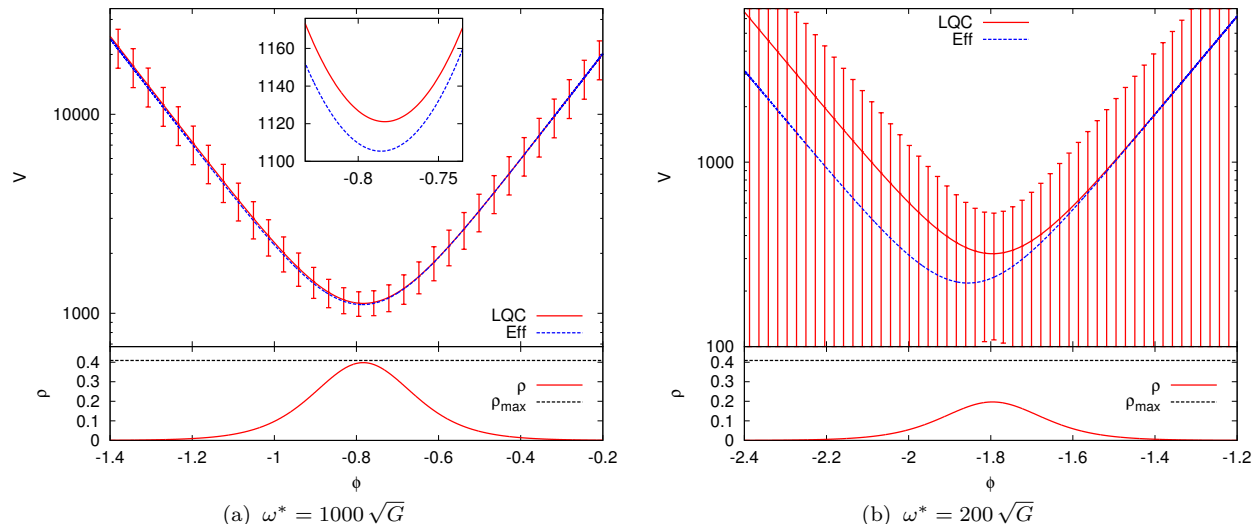


FIG. 15. Trajectories and energy densities for multip peaked-2 states with $\delta k = 2$ and different values of ω^* and η . Panel (a): $\omega^* = 1000\sqrt{G}$ and $\eta = 1 \times 10^{-4}$. Panel (b): $\omega^* = 200\sqrt{G}$ and $\eta = 2.5 \times 10^{-3}$. The solid (red) curves show the LQC trajectories, with the error bars representing the volume dispersion, and the dashed (blue) curves showing the corresponding effective trajectory.

($\Delta V/V = 1.17$), and there are significant differences between the LQC and the effective trajectory (Fig. 15(b)). The bottom panels in Fig. 15 show the evolution of the energy density ρ . We can see that in both of the cases ρ remains below the absolute maximum ρ_{\max} in sLQC (indicated with a dashed horizontal line in the figures). However, ρ gets very close to ρ_{\max} at the bounce for the state with $\omega^* = 1000\sqrt{G}$ which has smaller relative dispersion in volume. For the state with $\omega^* = 200\sqrt{G}$, which has larger relative dispersion in volume, the density at the bounce is much smaller than ρ_{\max} .

We now discuss the validity of the triangle inequalities for multip peaked-2 states. The evolution of the dispersion in volume $\Delta \ln(\hat{V})$ is shown for both cases in Fig. 16. It is clear that $\sigma_{\pm} + 2\sigma$ remains larger than $\Delta \ln(\hat{V})$ throughout the evolution in both cases, as predicted by the triangle inequality (2.16). Similarly to the case of multip peaked-1 states, 2σ is a constant of motion. Asymptotic values of the volume dispersions on both sides of the bounce are the same in both cases shown. Therefore, the horizontal curve for $\sigma_+ + 2\sigma$ and $\sigma_- + 2\sigma$ overlap. Another similarity with the multip peaked-1 states is that the difference in the asymptotic values of the relative fluctuations in volume is much smaller than unity for the range of parameters considered here, which, as before, results in the satisfaction of the stronger version of the triangle inequality (2.20) for both multip peaked-2 cases (Table II). As has been discussed above for the case of multip peaked-1 states, the reason, why highly non-Gaussian multip peaked-2 states satisfy this inequality, is tied to the way they are constructed, i.e. by using the phase factor $e^{-i\alpha}$ in eq.(3.2) which corresponds to “method-3” in Refs. [4, 30] and the particular choices for parameters of the state. It is important to note that whether (2.20) is satisfied depends on the details of the construction of the state and its parameters, however, all the states irrespective of the choice of parameters satisfy the triangle inequality (2.16).

V. DISCUSSION

The goal of our analysis was to understand the quantum evolution of squeezed and highly non-Gaussian states in LQC. We considered the spatially flat homogeneous and isotropic spacetime sourced with a massless scalar field in which the quantum Hamiltonian constraint takes the form of a Klein-Gordon equation, with the scalar field playing the role of internal time and where the spatial Laplacian is a quantum difference operator with uniform discreteness in volume. This model has been extensively studied using rigorous analytical and numerical techniques. The first results for this model, which established singularity resolution and the quantum bounce, were obtained using numerical simulations with Gaussian states initially sharply peaked on a classical trajectory [3, 4]. These studies brought out many important features of the new physics at the Planck scale. At curvatures very small compared to the Planck scale, the classical GR trajectory is an excellent approximation to the quantum dynamics. However, near the Planck scale, there are significant departures between the quantum and the classical evolution, and quantum geometric effects provide a non-singular bridge between the classically disjoint expanding and contracting branches.

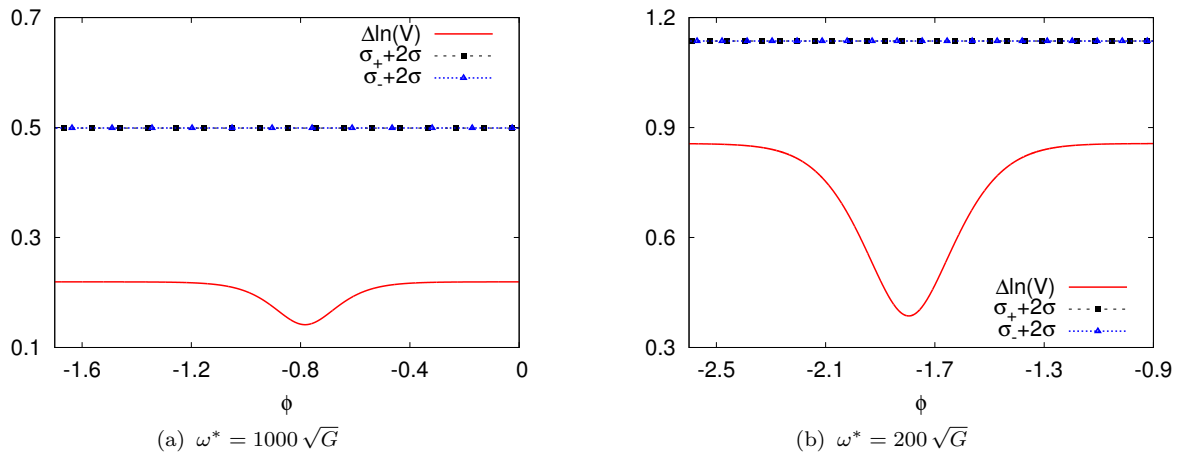


FIG. 16. Validity of the triangle inequality for multip peaked states with $\omega^* = 1000\sqrt{G}$ and $\eta = 1 \times 10^{-4}$ (panel(a)) and with $\omega^* = 200\sqrt{G}$ and $\eta = 2.5 \times 10^{-3}$ (panel(b)). In both cases $\delta k = 2$. The figure clearly demonstrate that $\sigma_{\pm} + 2\sigma$ (shown by horizontal curves) remains greater than $\Delta \ln(\hat{V})$ (shown by the solid red curve) throughout the evolution. The asymptotic values of the volume dispersions on both sides of the bounce are practically the same. Therefore, the horizontal curves for $\sigma_+ + 2\sigma$ and $\sigma_- + 2\sigma$ overlap.

The quantum bounce for sharply peaked states occurs at energy density $\rho_{\max} \approx 0.409\rho_{\text{Pl}}$ – the universal maximum for the energy density derived using an exactly solvable model in LQC [22]. It was found that the sharply peaked initial states remain sharply peaked throughout the evolution and the relative fluctuations of Dirac observables is strongly constrained across the bounce [23–26]. Quantum evolution of sharply peaked states further established that the evolution trajectory described by the expectation values of the physical observables is in excellent agreement with the one derived from the effective Hamiltonian. In recent years, this analysis has been generalized to a variety of models and numerical simulations of loop quantum universes with sharply peaked states for different choices of matter have been performed. However, an important issue for the robustness of the new physics in LQC is to understand the way quantum evolution is affected for states which are widely spread, are squeezed or are highly non-Gaussian. Although these states do not necessarily correspond to large classical universes at late times, they do belong to the physical Hilbert space. Therefore, to test the robustness of singularity resolution and the occurrence of the quantum bounce it is pertinent to ask the following questions: Do states that do not have any well defined peakedness properties at late times undergo a quantum bounce? What happens to the growth of fluctuations through the bounce? And finally, is the effective dynamics derived from the effective Hamiltonian (2.21), still a good approximation to the quantum evolution for highly squeezed and non-Gaussian states?

Numerical simulations with states which are widely spread or are highly squeezed or non-Gaussian is computationally very challenging due to the tremendously large integration domains involved and the associated stability constraints. To overcome these challenges, a numerical scheme called Chimera was recently developed. Its construction is based on an important property of the loop quantum difference equation – at large volumes, it is extremely well approximated by the differential Wheeler-DeWitt equation. Using a hybrid spatial grid, a sufficiently large inner grid where the evolution is governed by the quantum difference equation, and a carefully chosen outer grid where the Wheeler-DeWitt equation is solved, a significant reduction in computational time and a large increase in efficiency can be achieved. The Chimera scheme was recently used to study the evolution of widely spread Gaussian states [30]. It was found that while the qualitative features of the quantum bounce remain unaltered, various quantitative details of the quantum bounce depend on the choice of the initial state and their parameters. For these states it was found that, depending on the dispersion, there may be significant deviations between the LQC and the corresponding effective trajectory. Additionally, the energy density at the bounce can be much smaller than ρ_{\max} . As a general result, it was found that the effective theory always overestimates the energy density and underestimates the volume at the bounce.

In this work we used the Chimera scheme to study numerical evolutions of a wide range of states which depart, in some cases greatly, from Gaussianity. Moreover, some of these states have very large dispersion and no well defined peakedness properties. One of the main results of our analysis is that the quantum bounce occurs for all states, replacing the classical singularity, independently of the choice of parameters which control squeezedness and non-Gaussianity. During the entire evolution the expectation value of the volume observable remains non-zero and the energy density remains bounded irrespective of the initial state. Moreover, despite the non-Gaussian features, the

shape of the initial wavefunction is recovered when the energy density after the bounce becomes comparable to the value in the initial data. Our results show that the triangle inequalities on the relative fluctuations are satisfied across the bounce for a wide variety of squeezed and multi-peaked states. The triangle inequality derived in Ref. [24] is satisfied for all the states considered here, including the ones with multiple peaks. A version of this triangle inequality obtained under stronger assumptions for sharply peaked states in Ref. [25] is found to be violated for highly squeezed states. These results demonstrate for the first time that the quantum bounce is a property of far more general states than the Gaussian states and quantum fluctuations remain tightly constrained throughout the evolution, even for highly non-Gaussian states.

We find that the effective theory captures the main qualitative features of the quantum bounce quite well, and is a good approximation to LQC for states with small dispersion, even for states which significantly depart from Gaussianity. However, for states with large dispersion there are significant differences between an LQC trajectory and the corresponding effective trajectory. An important contrast between the effective theory and LQC is that, in the effective theory, the energy density at the bounce is always equal to the maximum upper bound, whereas, in the LQC evolution, the energy density at the bounce can be very small for highly squeezed and states with no well defined peakedness properties. In agreement with the recent results obtained in the analysis of widely spread Gaussian states [30], we find that the effective theory always overestimates the energy density and underestimates the volume at the bounce. This issue was analyzed in detail using squeezed states by studying the variation of the energy density at the bounce with the change in spread in the field momentum, which is directly related to the parameter η . We also found excellent agreement between our numerical results and the analytical calculations in Ref. [26], which was performed in the context of sLQC for states which are highly squeezed. In summary, these results on one hand indicate the conditions under which the effective description may not capture the underlying quantum evolution reasonably well, and on the other hand show a synergy between the numerical simulations of highly non-Gaussian states and the results from sLQC.

Based on the results obtained in this paper, it can be concluded that the quantum bounce is a robust feature of the spatially flat homogeneous and isotropic LQC with a massless scalar field, irrespective of the choice of the initial states. The effective theory, although showing deviations for states with large dispersions, is still able to capture the main qualitative features of the quantum bounce. The validity of the triangle inequalities demonstrates that the growth of the dispersion of the states across the bounce is tightly constrained, which presents very strong numerical evidences in support of cosmic recall [23] and discourages the speculations related to unbounded growth in the fluctuations of the state. Finally, the results from our numerical simulations turn out to be in complete synergy with the predictions of sLQC.

ACKNOWLEDGMENTS

We thank Ivan Agullo, Alejandro Corichi, Jorge Pullin and Edward Wilson-Ewing for comments. This work is supported by a grant from John Templeton Foundation and by NSF grant PHYS1068743. The opinions expressed in this publication are those of authors and do not necessarily reflect the views of John Templeton Foundation. BG acknowledges support from the Coates Scholar Research Award and the Dissertation Year Fellowship of the Louisiana State University. This material is based upon work supported by HPC@LSU computing resources.

REFERENCES

-
- [1] A. Ashtekar and P. Singh, “Loop Quantum Cosmology: A Status Report”, *Class.Quant.Grav.* **28** (2011) 213001, arXiv:1108.0893.
 - [2] A. Ashtekar, T. Pawłowski, and P. Singh, “Quantum nature of the big bang”, *Phys.Rev.Lett.* **96** (2006) 141301, arXiv:gr-qc/0602086.
 - [3] A. Ashtekar, T. Pawłowski, and P. Singh, “Quantum Nature of the Big Bang: An Analytical and Numerical Investigation. I.”, *Phys.Rev.* **D73** (2006) 124038, arXiv:gr-qc/0604013.
 - [4] A. Ashtekar, T. Pawłowski, and P. Singh, “Quantum Nature of the Big Bang: Improved dynamics”, *Phys.Rev.* **D74** (2006) 084003, arXiv:gr-qc/0607039.
 - [5] L. Szulc, “Open FRW model in Loop Quantum Cosmology”, *Class.Quant.Grav.* **24** (2007) 6191–6200, arXiv:0707.1816.
 - [6] W. Kaminski and J. Lewandowski, “The Flat FRW model in LQC: The Self-adjointness”, *Class.Quant.Grav.* **25** (2008) 035001, arXiv:0709.3120.

- [7] K. Vandersloot, “Loop quantum cosmology and the $k = -1$ RW model”, *Phys.Rev.* **D75** (2007) 023523, arXiv:gr-qc/0612070.
- [8] L. Szulc, W. Kaminski, and J. Lewandowski, “Closed FRW model in Loop Quantum Cosmology”, *Class.Quant.Grav.* **24** (2007) 2621–2636, arXiv:gr-qc/0612101.
- [9] E. Bentivegna and T. Pawłowski, “Anti-deSitter universe dynamics in LQC”, *Phys.Rev.* **D77** (2008) 124025, arXiv:0803.4446.
- [10] W. Kaminski and T. Pawłowski, “The LQC evolution operator of FRW universe with positive cosmological constant”, *Phys.Rev.* **D81** (2010) 024014, arXiv:0912.0162.
- [11] T. Pawłowski and A. Ashtekar, “Positive cosmological constant in loop quantum cosmology”, *Phys.Rev.* **D85** (2012) 064001, arXiv:1112.0360.
- [12] T. Pawłowski, R. Pierini, and E. Wilson-Ewing, “Loop quantum cosmology of a radiation-dominated flat FLRW universe”, arXiv:1404.4036.
- [13] A. Ashtekar, T. Pawłowski, and P. Singh, “Pre-inflationary dynamics in loop quantum cosmology”, (*To appear*).
- [14] P. Diener, B. Gupt, M. Megevand, and P. Singh (*To appear*).
- [15] A. Ashtekar and E. Wilson-Ewing, “Loop quantum cosmology of Bianchi I models”, *Phys.Rev.* **D79** (2009) 083535, arXiv:0903.3397.
- [16] A. Ashtekar and E. Wilson-Ewing, “Loop quantum cosmology of Bianchi type II models”, *Phys.Rev.* **D80** (2009) 123532, arXiv:0910.1278.
- [17] E. Wilson-Ewing, “Loop quantum cosmology of Bianchi type IX models”, *Phys.Rev.* **D82** (2010) 043508, arXiv:1005.5565.
- [18] D.-W. Chiou, “Loop Quantum Cosmology in Bianchi Type I Models: Analytical Investigation”, *Phys.Rev.* **D75** (2007) 024029, arXiv:gr-qc/0609029.
- [19] M. Martín-Benito, G. Mena Marugan, and T. Pawłowski, “Loop Quantization of Vacuum Bianchi I Cosmology”, *Phys.Rev.* **D78** (2008) 064008, arXiv:0804.3157.
- [20] D. Brizuela, D. Cartin, and G. Khanna, “Numerical techniques in loop quantum cosmology”, *SIGMA* **8** (2012) 001, arXiv:1110.0646.
- [21] P. Singh, “Numerical loop quantum cosmology: an overview”, *Class.Quant.Grav.* **29** (2012) 244002, arXiv:1208.5456.
- [22] A. Ashtekar, A. Corichi, and P. Singh, “Robustness of key features of loop quantum cosmology”, *Phys.Rev.* **D77** (2008) 024046, arXiv:0710.3565.
- [23] A. Corichi and P. Singh, “Quantum bounce and cosmic recall”, *Phys.Rev.Lett.* **100** (2008) 161302, arXiv:0710.4543.
- [24] W. Kaminski and T. Pawłowski, “Cosmic recall and the scattering picture of Loop Quantum Cosmology”, *Phys.Rev.* **D81** (2010) 084027, arXiv:1001.2663.
- [25] A. Corichi and E. Montoya, “On the Semiclassical Limit of Loop Quantum Cosmology”, *Int.J.Mod.Phys.* **D21** (2012) 1250076, arXiv:1105.2804.
- [26] A. Corichi and E. Montoya, “Coherent semiclassical states for loop quantum cosmology”, *Phys.Rev.* **D84** (2011) 044021, arXiv:1105.5081.
- [27] D. A. Craig and P. Singh, “Consistent probabilities in loop quantum cosmology”, *Class.Quant.Grav.* **30** (2013) 205008, arXiv:1306.6142.
- [28] V. Taveras, “Corrections to the Friedmann Equations from LQG for a Universe with a Free Scalar Field”, *Phys.Rev.* **D78** (2008) 064072, arXiv:0807.3325.
- [29] P. Singh, “Loop cosmological dynamics and dualities with Randall-Sundrum braneworlds”, *Phys.Rev.* **D73** (2006) 063508, arXiv:gr-qc/0603043.
- [30] P. Diener, B. Gupt, and P. Singh, “Numerical simulations of a loop quantum cosmos: robustness of the quantum bounce and the validity of effective dynamics”, arXiv:1402.6613.
- [31] P. Diener, B. Gupt, and P. Singh, “Chimera: A hybrid approach to numerical loop quantum cosmology”, *Class.Quant.Grav.* **31** (2014) 025013, arXiv:1310.4795.
- [32] G. A. Mena Marugan, J. Olmedo, and T. Pawłowski, “Prescriptions in Loop Quantum Cosmology: A comparative analysis”, *Phys.Rev.* **D84** (2011) 064012, arXiv:1108.0829.
- [33] A. Ashtekar, J. Lewandowski, D. Marolf, J. Mourao, and T. Thiemann, “Quantization of diffeomorphism invariant theories of connections with local degrees of freedom”, *J.Math.Phys.* **36** (1995) 6456–6493, arXiv:gr-qc/9504018.
- [34] D. Marolf, “Refined algebraic quantization: Systems with a single constraint”, arXiv:gr-qc/9508015.
- [35] J. Willis, “On the low energy ramifications and a mathematical extension of loop quantum gravity”, *PhD, The Pennsylvania State University*, 2004.
- [36] D. Craig and P. Singh, “Consistent Histories in Quantum Cosmology”, *Found.Phys.* **41** (2011) 371–379, arXiv:1001.4311.
- [37] D. A. Craig and P. Singh, “Consistent Probabilities in Wheeler-DeWitt Quantum Cosmology”, *Phys.Rev.* **D82** (2010) 123526, arXiv:1006.3837.
- [38] D. A. Craig, “Dynamical eigenfunctions and critical density in loop quantum cosmology”, *Class.Quant.Grav.* **30** (2013) 035010, arXiv:1207.5601.